







Theoretical study of stability, epitaxial formation, and phase transformations of two-dimensional pnictogen allotropes

Conor Hogan ^{1,2,*}, Pierre Lechiffart ^{2,3}, Simone Brozzesi,² Sofiya Voronovich-Solonevich,⁴ Alexander Melnikov ⁴, Roberto Flammini ¹, Simone Sanna ^{5,6} and Kris Holtgrewe ^{5,6,†}

¹*Istituto di Struttura della Materia-CNR (ISM-CNR), Via del Fosso del Cavaliere 100, 00133 Rome, Italy*


²*Dipartimento di Fisica, Università di Roma “Tor Vergata”, Via della Ricerca Scientifica 1, 00133 Rome, Italy*

³*CNRS/Aix-Marseille Université, Centre Interdisciplinaire de Nanoscience de Marseille UMR 7325, Campus de Luminy, 13288 Marseille Cedex 9, France*

⁴*Research Institute for Nuclear Problems, Belarusian State University Bobruiskaya str., 11 220006 Minsk, Belarus*

⁵*Institut für Theoretische Physik, Justus-Liebig-Universität Gießen, 35392 Gießen, Germany*

⁶*Center for Materials Research (LaMa), Justus-Liebig-Universität Gießen, 35392 Gießen, Germany*

 (Received 14 July 2021; revised 25 November 2021; accepted 6 December 2021; published 20 December 2021)

We present a theoretical study of the thermodynamical factors that determine epitaxial formation of single layer 2D pnictogen (P, As, Sb, Bi) allotropes on substrates of any type. The interplay of substrate-adlayer interaction and strain induced by epitaxial matching is analyzed in terms of the phase diagram describing growth during the gaseous deposition stage. The necessary conditions to favor particular allotrope growth (in particular, the α and β phases) are determined. We show that buckled Sb and Bi layers can overcome large tensile strain and form flat honeycomb layers even on common metal surfaces. An alternative strategy for controlled allotrope formation via thermally induced phase transformations between α and β phases is examined in detail, including important methodological analysis. All four elements follow reconstructive transition pathways, whose activation barrier correlates with the bond dissociation energy. If nucleation is considered, the barrier can further reduce by about 13% and thus becomes quite accessible under typical annealing conditions. The role of van der Waals and spin-orbit corrections in the stability of several allotropes is carefully addressed. The theoretical insight gained is evaluated in light of experimental reports and strategies for controlling growth are outlined.

DOI: [10.1103/PhysRevB.104.245421](https://doi.org/10.1103/PhysRevB.104.245421)

I. INTRODUCTION

The discovery of graphene and other single layer group-IV elemental honeycomb structures [1] has driven a search for new isostructural forms of group-VA (group 15, pnictogen) elements. Elemental two-dimensional (2D) layers of P, As, Sb, and Bi are stable semiconductors and thus attractive for various device applications [2–6] and as components in van der Waals (vdW) heterostructure design [7,8]. Their tunable electronic, optical, catalytic, and electrochemical properties offer wide potential for technologies ranging from drug delivery to transistors [5]. Several reviews on the properties and synthesis of the 2D pnictogen family have already appeared [5,6,9–11] as well as focused reviews of their relevance for topological materials [4], electrical transport [12], field effect transistors [13], functionalization [14,15], electrochemistry [16], and epitaxial growth [17].

Due to the possibility to form hybridized and unhybridized bonds and electron lone pairs, the 2D pnictogens are able to adopt a large number of allotropic forms. Of these, the α and β phases (Fig. 1) occur naturally in pseudolayered bulk crystals such as black phosphorus and gray arsenic [3]. While both are constructed of repeated buckled-honeycomb

motifs, the α phase exhibits a puckered (washboardlike) or double-layered structure, while the β is a low-buckled phase similar to silicene, germanene, and stanene [18,19]. From a theoretical perspective, α and β phases of P, As, Sb, and Bi in their freestanding layer form are predicted to be stable [6]. The various allotropes offer a rich ensemble of physical and electronic properties for exploitation (symmetry, band gap, tunability, topology, stability), driving the huge interest in controlling their experimental preparation.

Synthesis of high-quality single layers remains a significant experimental challenge, however. In particular, the experimental realization of α -phosphorene by exfoliation of black phosphorus attracted huge interest [20,21] and has led to exciting applications [22]. Hereon, the notation α -P, β -As, etc., indicates a 2D allotrope; we reserve the suffix -ene for 2D geometries comprising (distorted) hexagons. However, as exfoliated samples are typically several layers thick, much effort has been made in growing ultrathin sheets by means of epitaxial growth techniques. In fact, single layer β phases of these four elements have been prepared on surfaces by thermal evaporation and annealing. While β phases of Sb and Bi are reported to form on various metallic (111) surfaces and selenide/telluride substrates, growth of continuous β -P and β -As sheets appears considerably more difficult and has only been reported for a handful of systems [23–25]. Regarding the α phase, epitaxial growth has only been reported for Sb (again, on chalcogenides) and Bi (on a variety of

*conor.hogan@ism.cnr.it

†kris.holtgrewe@theo.physik.uni-giessen.de

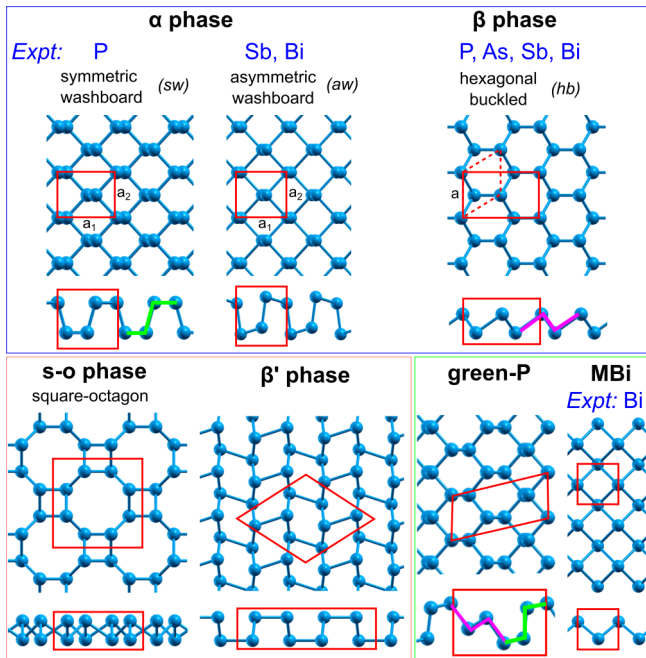


FIG. 1. Top and side views of the 2D pnictogen allotropes studied in this work. Simulation cells are indicated by solid red boxes. Construction of green-P from fragments of α and β is indicated by colored lines.

nonmetallic surfaces). An intriguing alternative strategy for controlling growth is to induce a transition from one allotrope to another, as initially proposed for phosphorene [26]. In fact, recent works have reported thermally induced phase transformations between α and β allotropes for antimonene grown on Bi_2Se_3 and SnSe substrates [27,28] and bismuthene on $\text{Cu}_2\text{O}_3/\text{Cu}(111)$ [29]. This annealing process offers an alternative route to precisely control the allotrope formation.

The current paper aims to provide insight into the thermodynamical factors that determine the epitaxial formation of monolayer 2D pnictogen allotropes by means of systematic, first-principles calculations. Epitaxial growth is a complicated and multifaceted process controlled by many factors, including strain and lattice matching, use of alloys as buffer layers, strength and character of interfacial interactions [17,30], as well as the growth parameters themselves [31,32] (temperature and pressure, kinetic factors such as sticking coefficients, nucleation, etc.). While relative stability of specific pnictogen/substrate combinations has been investigated in various theoretical works [33–35], the calculation of the phase diagram for the growth process itself and its modification due to strain from lattice mismatch is a complex task that has not been addressed. We explain why the α allotrope is generally favored during deposition and what energetic conditions are necessary to favor other phases. Moreover, the potential for inducing phase transformations of an adsorbed monolayer via annealing has not been evaluated for all pnictogens, and the precise path this transition must take has not been fully explored. A careful analysis of the methodology needed to accurately describe the phase transition is provided, which reveals large uncertainties in the published data as well as a general overestimation of transition barriers. The theoretical

analysis provided here helps to explain and interpret many experimental reports to date of preparation of 2D pnictogen monolayers and will guide future synthesis.

The paper is organized as follows. Section II focuses on calculations of the freestanding 2D monolayer pnictogens. After outlining some methodological aspects, the relative stability of the layers is examined via careful consideration of vdW interactions and spin-orbit coupling, and technical aspects of simulating phase transformations between allotropes are examined. Section III analyzes the phase diagram for epitaxial formation during a deposition process. Simple thermodynamical expressions are derived to describe the favored phases. The impact of low and high strain within the adlayers is investigated. Section IV analyzes 2D monolayer formation under annealing conditions and in particular the barriers that determine possible phase transformations. An overview of the pertinent theoretical results available from the literature and their connection with experimental evidence is given in Sec. V. The paper concludes with a brief outlook and suggestions for tuning the formation of 2D pnictogen allotropes.

II. FREESTANDING LAYERS

A. DFT simulations: Geometry

Calculations of geometries and total energies of various freestanding 2D structures were computed using density functional theory (DFT) within the plane-wave/pseudopotential framework, as implemented in the quantum-ESPRESSO suite [36]. Optimized norm-conserving DOJO-type pseudopotentials were used along with recommended kinetic energy cutoffs of 44 Ry (P), 84 Ry (As), 86 Ry (Sb), and 66 Ry (Bi) [37,38]. Spin-orbit coupling was included in selected calculations of Sb and Bi. Sheets were modelled using supercells of height 20 Å.

Geometries were optimized using the variable cell relaxation (vc-relax) option of quantum-ESPRESSO, allowing the cell lattice parameters and angles to vary freely within the 2D plane. Atomic positions were optimized until forces fell below 10 meV/Å. Various exchange correlation (XC) and vdW schemes were used as discussed in the following section.

Thanks to several studies using high throughput computing and random search algorithms, a large number of possible 2D geometries for the group 15 elements has been identified [39,40]. However, many of these structures are saddle points of the energy landscape, as suggested by the presence of imaginary frequencies. In this work we consider the seven geometries shown in Fig. 1. Two of these have been widely observed experimentally. These are the hexagonal buckled (*hb*) β phase (observed for all four elements) and the *p*-monoclinic puckered symmetric washboard (*sw*) or asymmetric washboard (*aw*) geometries of the α phase (observed in phosphorene, antimonene, and bismuthene). A square ‘MBi’ phase has been reported experimentally for Bi on top of an α -Bi substrate [41]. We also consider three structures recently proposed from theoretical grounds. The square-octagonal (*s-o*) phase has been shown to be dynamically stable for all four pnictogens [42]. An oblique β' phase identified by Singh *et al.* [43] (referred to as β in that work) is predicted to be stable at least in bismuthene. Finally, green phosphorene [44]

TABLE I. Lattice constants for the α and β phases and surface atomic density of freestanding monolayer 2D pnictogen allotropes, as calculated with DF2-B86R. For the ‘green-P’ phase, the density lies between those of β and α by construction and is not shown.

	Lattice constant (Å)		Density (atoms/Å ²)					MBi
	α (a_1, a_2)	β (a)	α	β	s-o	β'		
P	4.55	3.31	3.28	0.27	0.22	0.17	0.23	0.22
As	4.67	3.67	3.58	0.23	0.18	0.16	0.19	0.19
Sb	4.71	4.34	4.10	0.20	0.14	0.12	0.15	0.15
Bi	4.79	4.54	4.30	0.18	0.13	0.11	0.15	0.13

has a corrugated geometry that resembles a combination of α and β phases (see colored lines in Fig. 1) and has attracted interest, e.g., for gas sensing [45]. For the 2D systems, k -point sets of $15 \times 15 \times 1$ (α , β , MBi), $9 \times 15 \times 1$ (green-P), and $8 \times 8 \times 1$ (β' and s-o) were used.

B. Stability of freestanding pnictogen sheets

Cohesive energies of freestanding (FS) sheets containing N atoms per cell are computed according to

$$\varepsilon_X^{\text{coh}} = -(E_X^{\text{FS}} - N\varepsilon^{\text{atom}})/N, \quad (1)$$

where X indicates a pnictogen allotrope (α -P, β -Sb, etc.), E_X^{FS} is the DFT total energy (per cell), and $\varepsilon^{\text{atom}}$ is the energy of the isolated atom (computed using noncubic cells and including spin polarization). We adopt the standard convention, whereby formation energies are typically negative while cohesive and adsorption energies are typically positive [6].

Optimized geometries for the allotropes in Fig. 1 were computed for P, As, Sb, and Bi, using a number of XC functionals and vdW interaction schemes. Computed lattice parameters are in general agreement with previous calculations where available (an excellent summary is given in Ersan *et al.* [6]). Many early studies of 2D pnictogens adopted the PBE functional [46] only. As previously noted for phosphorene [47] and antimonene [27], however, vdW corrections are important even in these single layered puckered/buckled systems due to considerable nonbonding interactions within the layers. Hence we have also considered the semiempirical D2 correction [48] as well as more advanced nonlocal vdW functionals [49–53]. In particular we consider here the vdW-DF-ob86 (optB86b) approach [54], found to yield optimal lattice parameters for phosphorene [47], and the revised vdW-DF2-B86R functional [55], recently demonstrated to yield excellent overall performance for describing both weakly bound and strongly bound solids, including intralayer lattice constants in layered systems [56]. In particular, DF2-B86R is reported to yield lattice parameters for arsenene in excellent

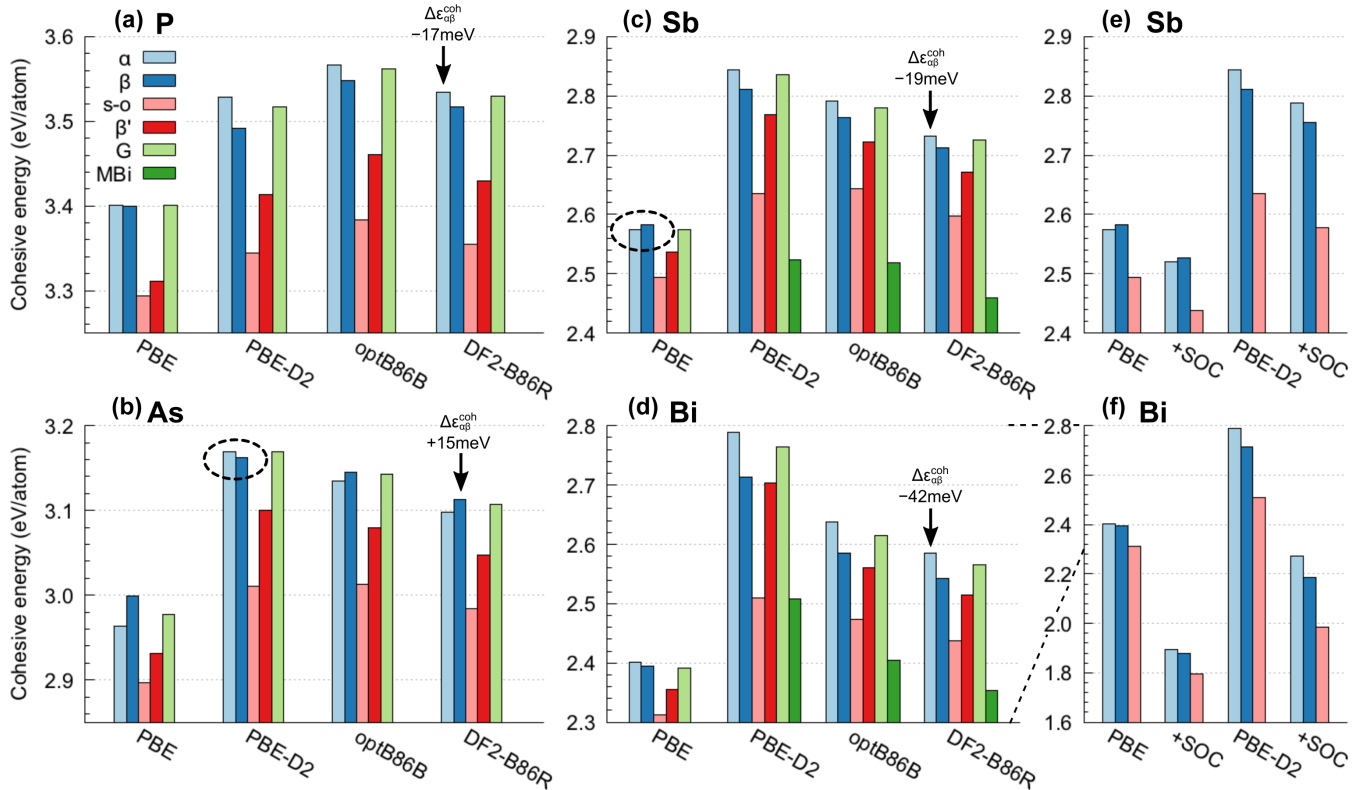


FIG. 2. Cohesive energies of the allotropes shown in Fig. 1 for (a) P, (b) As, (c) Sb, and (d) Bi computed using different van der Waals treatments (see text) and neglecting spin-orbit coupling. ‘Green’ phosphorus structure is indicated by ‘G.’ Arrows indicate the most stable phase for each element according to DF2-B86R. The energy difference between α and β phases, $\Delta\varepsilon_{\alpha\beta}^{\text{coh}} = \varepsilon_{\beta}^{\text{coh}} - \varepsilon_{\alpha}^{\text{coh}}$, is indicated. Some MBi data lie outside the chosen energy ranges. Panels (e) and (f) show values for Sb and Bi only, using PBE and PBE-D2 functionals with and without spin-orbit coupling. Note the change of scale between panels (d) and (f).

agreement (to within 0.1 Å) with accurate diffusion quantum Monte Carlo (DMC) calculations [57]. Lattice constants for α and β phases computed with DF2-B86R are listed in Table I.

Figures 2(a)–2(d) report the cohesive energies ε^{coh} for the four pnictogens as a function of the XC functional and van der Waals correction. Adding a vdW correction can change ε^{coh} by as little as 40 meV (P, s-o phase) or as much as 390 meV (α -Bi). With the exception of the P allotropes, PBE and PBE-D2 yield lower and upper bounds to the cohesive energies. The nonlocal-vdW methods yield quite similar intermediate values, with DF2-B86R consistently lower by about 30–60 meV. The semiempirical PBE-D2 corrects the PBE results adequately in the lighter pnictogens but appears to overestimate the values for Sb and especially Bi. Trends in relative stability are mostly consistent, and there are only two aberrations: The values for the α and β phases are inverted for Sb in the PBE approach and for As in the PBE-D2 approach [marked by dashed ovals in Figs. 2(b) and 2(c)]. All four XC/vdW treatments find the s-o and β' phases relatively unstable with respect to the β and α phases. The ‘green’ allotrope as expected yields energies intermediate to those of β and α phases. Based on the nonlocal DF2-B86R results, therefore, the most stable 2D phase for P, Sb, and Bi is the α phase. For As, the β phase is most stable. This finding for As is in agreement with the DMC calculations [57], which find a larger energy difference (+34 meV) but consistently smaller (by about 0.3 eV) cohesive energies for α and β phases. We remark that a widely cited study of these four systems used PBE (without vdW) and concluded that the β allotrope is more stable for As, Sb, and Bi [3]. These conclusions clouded several subsequent interpretations of experimental studies.

Spin-orbit coupling is expected to play an important role in the geometries and cohesive energies for the heavier elements. In Figs. 2(e) and 2(f) we compare cohesive energies using PBE and PBE-D2 for α , β , and s-o geometries, with and without inclusion of SOC. Indeed, SOC results in changes in the absolute cohesive energies of up to 50 meV in Sb and 500 meV in Bi. However, it does not change the relative cohesive energies of the different phases. It should therefore be reasonable to omit SOC when performing calculations that rely on relative energies, such as transition pathways, or when interpreting relative stabilities of other possible allotropic phases.

C. Phase transformation pathway simulation

In order to simulate the minimum energy path (MEP) of a phase transformation between the two most stable freestanding allotropes (α and β) we adopt the variable-cell nudged elastic band method (vcNEB) [58], including climbing images [59], as implemented in the USPEX code [60]. Total energies and stresses of each image are computed with quantum-ESPRESSO. Spin-orbit coupling is neglected.

In a previous study [27] we examined two kinds of $\alpha \rightarrow \beta$ phase transformation for the case of antimonene. The first pathway, called the ‘bond-flipping path’ (BFP) constitutes a displacive transformation in which no bonds are broken. Instead, some bonds connecting the hexagonal units in the puckered α structure flip or rotate to form the buckled β structure. This results in a transfer of atoms between upper

and lower layers of the respective structures. The second pathway, called the ‘bond-breaking path’ (BBP), constitutes a reconstructive transformation in which atoms in the upper and lower layers rearrange without leaving their respective layer. Both pathways are illustrated in Fig. 3(b). Similar paths have been proposed elsewhere for P-ene, Sb-ene, and very recently Bi-ene [26,28,29,47].

While the BFP is obvious from inspection of the two lattices, the BBP is not easily determined. Since the final path depends on the initial choice of mapping between atoms in the two phases, it is important to consider other pathways. This is complicated in periodic systems due to the multitude of possibilities, although efficient algorithms have been proposed [61,62]. We adopt a simple scheme that allows us to distinguish between displacive and reconstructive pathways. For each $\alpha \rightarrow \beta$ mapping M (consider a cell with four atoms) we compute the following quantity:

$$D_M^{\text{tot}} = \sum_{i=1}^4 |\mathbf{r}_{i,M}(\beta) - \mathbf{r}_i(\alpha)|. \quad (2)$$

For each atom, we compute the difference between the cartesian positions in the final geometry β and in the initial geometry α . We then sum over the atoms in the unit cell and obtain the distance D_M^{tot} traveled by all atoms, which is different for each mapping M . An analogous term D_M^{vert} describes the sum over vertical displacements only. Atoms are allowed to displace by one lattice vector at most, and specific rotations of the hexagonal β cell are considered.

A summary of the mappings is shown in Fig. 3(a). The data is reported for the case of Sb-ene, although other pnictogens yield similar results. The picture shows that many different paths of different total and vertical displacement are possible and should be considered. The mappings roughly group into two domains representing reconstructive bond-breaking paths (small D_M^{vert}) and displacive bond-flipping paths (larger D_M^{vert}). Further domains appear at even larger vertical displacements than shown here and correspond to pathways where two or more bonds are flipped. The BBP group contains the mappings with minimum total displacement.

The two ‘original’ pathways correspond to those proposed by some of us for antimonene [27]. We performed vcNEB calculations of several other mappings in the vicinity of these two points. We found that many of the alternatives lead to energetically equivalent paths, typically by means of an initial step whereby the α geometry reverses its buckling direction or is simply rotated by 90°. An example for the latter can be seen at the beginning of the pathway in Fig. 3(c). Other paths consistently led to higher barrier heights. We thus confirm that the original two pathways in Ref. [27] are indeed the optimal ones, at least within the approximations of our method.

Although this approach helps to reduce the mapping space to a tractable number of possible pathways, care must nonetheless be taken during the simulation to identify the correct MEP. This is illustrated in Fig. 3(c). If the number of images is too low, the simulation can predict too high energy barriers (red line, 40 images, transition state at E'). By extending the explored space to 71 images a better MEP can be identified [blue line, terminating at the (equivalent) rotated geometry β_2 , highest barrier at B]. For the specific

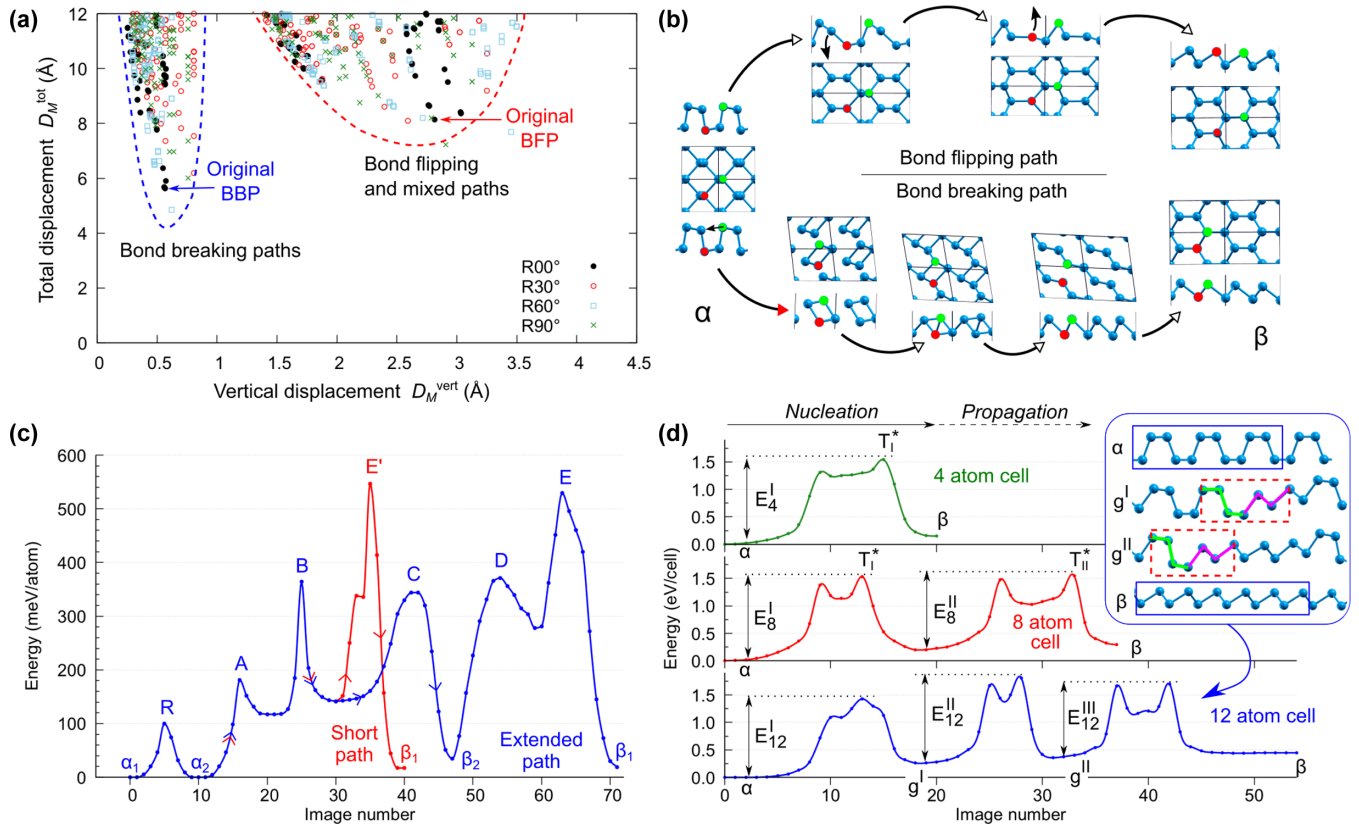


FIG. 3. Calculation of the minimum energy pathway (MEP) for the $\alpha \rightarrow \beta$ transformation in 2D pnictogens. (a) Total versus vertical displacements for Sb-ene for different initial (α) and final (β) atomic configurations. Four possible rotations of the β cell are considered. ‘Original’ refers to paths discussed in Ref. [27]. (b) Schematic of the bond-breaking and bond-flipping paths. (c) Pathway dependence on number of images, illustrated for phosphorene (DF2-B86R functional). The shorter pathway ABE’ (red) from α_1 to β_1 has a maximum barrier at point E' . The extended pathway ABCDE reveals a lower barrier at point B when truncated at the (equivalent) rotated geometry β_2 . R indicates a simple 90° rotation of the initial α_1 cell to α_2 . (d) Transition pathway as a function of simulation cell size, as computed for phosphorene (PBE-D2). Geometries at local minima for the 12-atom cell case are shown in the inset. The dashed red box indicates the green phosphorene structure (cf. Fig. 1). The local barriers for successive steps I–II–III are $E_4^I = 1.55$; $E_8^I = 1.55$, $E_8^{II} = 1.35$; $E_{12}^I = 1.45$, $E_{12}^{II} = 1.55$, $E_{12}^{III} = 1.35$ (in eV/cell).

system shown here (the $\alpha \rightarrow \beta$ transition in phosphorene using the DF2-B86R functional), the error can be as large as 200 meV/atom. Typical calculations in the literature implement fewer than ten images.

Finally, we consider an important choice in the simulation that has hardly been considered in previous works: the cell size. Previous simulations of the $\alpha \rightarrow \beta$ transition adopted an orthorhombic four-atom cell. Figure 3(d) demonstrates the change in pathway and barrier height for a BFP-type transition in phosphorene as the simulation cell is expanded to eight and 12 atoms. To keep the simulations tractable, a reduced cutoff (30 Ry) and k -point grid has been used here. The transition is found to occur in a wavelike motion with local bond-flipping events (pulses) occurring in successive cells. It is interesting to note that, in intermediate steps, the green phosphorene phase is found locally (compare g^I and g^{II} with Fig. 1). This suggests it may indeed be possible to stabilize the green-P phase by thermally inducing a phase transformation on an appropriately corrugated or vicinal substrate, as noted in Refs. [33,44].

Within the limits of accuracy of our simulations, the height of the first pulse due to the $\alpha \rightarrow \beta$ transformation in the first unit cell is independent of the size of the supercell ($E_{4,8,12}^I =$

1.45–1.55 eV/cell). Instead, the barrier for the flipping event in the last cell ($E_8^{II} = E_{12}^{III} = 1.35$ eV/cell) is notably reduced by about 13% with respect to the preceding pulse. The cell-by-cell transformation thus corresponds in the experimental system to a ‘nucleation-propagation’ process [28]. It is important to note, however, that the reduction of 13% in pulse height implies that each pulse is mostly, but not completely, independent of the others. Under these conditions, the activation energy (Gibbs free energy) can be renormalized by the number of atoms per *interacting unit* (i.e., four atoms) but not per *simulation cell* (otherwise the final barrier height in eV/atom would simply tend to zero for very large simulation cells). For this reason, our computed barrier for the α -P \rightarrow green-P transformation ($=E_8^I = 0.39$ eV/atom) is about double that obtained by Han *et al.* [44] ($E_b = 0.21$ eV/atom) by renormalizing over all atoms in a cell containing two units of green-P. Similarly, a very low barrier of ~ 150 meV/atom was reported by Shi *et al.* [28] for an $\alpha \rightarrow \beta$ -like transformation in a 12-atom cell of Sb-ene. If only the four atoms involved in local bond-flipping events are considered during the rescaling, a more realistic barrier of ~ 450 meV/atom is obtained (a value of 160 meV/atom would also be obtained

here for 12-atom P-ene, if a similar artificial rescaling were performed). As shown in Fig. 3(d), however, the true reduction in subsequent barrier heights due to nucleation processes is much lower, at about 13%.

III. STABILITY UNDER EPITAXIAL GROWTH CONDITIONS

In the previous section we showed that for isolated, freestanding 2D sheets, the α phase is the most stable for the case of P, Sb, and Bi, whereas for As the β phase is most stable. The favored structure in an epitaxial growth scenario may be quite different, however, due to a large range of factors including substrate interaction, temperature and pressure, kinetic effects, and strain.

In this section we will discuss a few general conditions that determine single layer epitaxial growth based on first-principles thermodynamics. A detailed description for the case of antimonene synthesis on bismuth selenide has been provided by some of us in a previous work [27], and some of the concepts are recalled here. During the deposition stage, the system is described as a substrate of constant area A interacting with a gaseous reservoir of pnictogen molecules. The formation energy of a particular 2D phase is defined *per area* and obtained from the grand (Landau) potential as

$$\gamma(\mu) = (U - TS - \mu N)/A. \quad (3)$$

Here U is the internal energy (approximated by the DFT total energy) and S the entropy; the temperature T is kept constant. The chemical potential μ is also constant (but unknown) and is determined by the vapor partial pressure at the given temperature. In the following we will neglect the TS term which should be of rather similar magnitude for both phases being structurally related in terms of the hexagons that build up the 2D structure. Because we are interested in formation energy differences, the entropy term should cancel out [27]. Indeed, Tristant *et al.* [47] reported differences of less than 10 meV/atom at 300 K between the entropic contributions of α -P and β -P; other studies on arsenene suggest the difference could be substantially higher, however [63].

We consider the formation of a 2D sheet of some phase X (where X is a pnictogen allotrope) on a substrate using a deposition process. The formation energy per area for the heterostructure, relative to that of the clean substrate, is

$$\Delta\gamma = (E_{X/\text{sub}} - E_{\text{sub}} - \mu N)/A, \quad (4)$$

where $E_{X/\text{sub}}$ and E_{sub} are the total energies of the heterostructure and substrate, respectively, and μ is the chemical potential of the pnictogen. By plotting the (unknown) parameter μ on the x axis and the function $\Delta\gamma(\mu)$ on the y axis, Eq. (4) yields the phase diagram describing the formation of different allotropes on a particular surface exposed to a constant vaporous particle reservoir. The total energies can be directly accessed by first-principles simulations. In practice, it requires identification of suitable supercell geometries to describe lattice matched and incommensurate phases. In the following we discuss a simplified model to illustrate some general principles.

We first consider the case of freestanding sheets, i.e., epitaxial growth in the limit of very weak interaction with the

substrate. The formation energies for α and β phases for the four pnictogens are plotted in Fig. 4(a). The s -o, β' , and MBi phases are not favored at reasonable values of μ and are thus not considered. While the green allotrope is, by design, energetically competitive in freestanding form, it is highly unlikely to remain so after epitaxial growth on a typical substrate and is thus not explicitly considered in the following analysis. For large values of μ (pnictogen-rich), the favoured phase is determined solely by the slope (i.e. the value of N/A for that phase). In other words, monolayer phases that pack more atoms into the same area should be favored in the deposition phase. As Table I shows, this always corresponds to the α phase. Based solely on thermodynamic principles, therefore, it should be possible to synthesise an α phase monolayer of any pnictogen during a deposition process by tuning μ via T and partial pressure. (Note this refers only to *monolayers*: multilayer β growth may occur before conversion to α , depending on the complete phase diagram and experimental conditions, see, e.g., Ref. [64]).

Figure 4(a) also demonstrates that, under very weakly bound conditions, it should only be possible to form the β phase in the case of arsenic (and only in a narrow range of chemical potential). The probability to favor the β phase is determined by the crossing point of the α and β formation energies. For simplicity, we consider unit cells of α and β phases having the same number of atoms (i.e., $N = 4$). The y value of the crossing point $\Delta\gamma^*$ [see Fig. 4(a)] is then given by

$$\Delta\gamma^* = \Delta\gamma^{\text{FS}} = \frac{E_{\alpha}^{\text{FS}} - E_{\beta}^{\text{FS}}}{A_{\alpha} - A_{\beta}}, \quad (5)$$

where E_X^{FS} is the total energy of the freestanding phase X . The range of μ for which the β phase is favored over the α is thus

$$\Delta\mu^* = -\frac{A_{\beta}}{N} \Delta\gamma^*. \quad (6)$$

Note that $A_{\alpha} < A_{\beta}$ under reasonable strain conditions; the sign and value of $E_{\alpha}^{\text{FS}} - E_{\beta}^{\text{FS}}$ can be read from Fig. 2. If $\Delta\gamma^* > 0$, the β phase is unstable for every value of μ .

As $\Delta\gamma^*$ depends on total energy and area, we can immediately consider the impact of strain when matching the freestanding sheet to a substrate. It is useful to compare the isotropically strained β phase to the unstrained α phase, since the latter's rectangular cell is harder to match on a substrate. Changes in total energy due to strain are reported in Fig. 5(a) for the four pnictogens. Although similar curves have been reported before (as energy per atom), it is interesting to note that the differences among various elements are amplified when plotting the energy *per area* (note in particular the comparatively low energy penalties for Sb and Bi at high strains). The impact on the phase diagram is shown in Fig. 5(b), for the extreme cases of $\pm 10\%$ strain. The calculations show that for Bi and Sb the effect of $+10\%$ tensile strain on $\Delta\gamma^*$ is actually fairly minor (the value roughly doubles at $+20\%$). Instead, the β phases of P and As exhibit a much larger sensitivity to strain. Moreover, an interesting feature that emerges from Eq. (5) is that compressive strain causes A_{β} to approach the value of A_{α} , causing a step increase in the value of $\Delta\gamma^*$. Coupled with the steeper profiles in the energy vs strain curves,

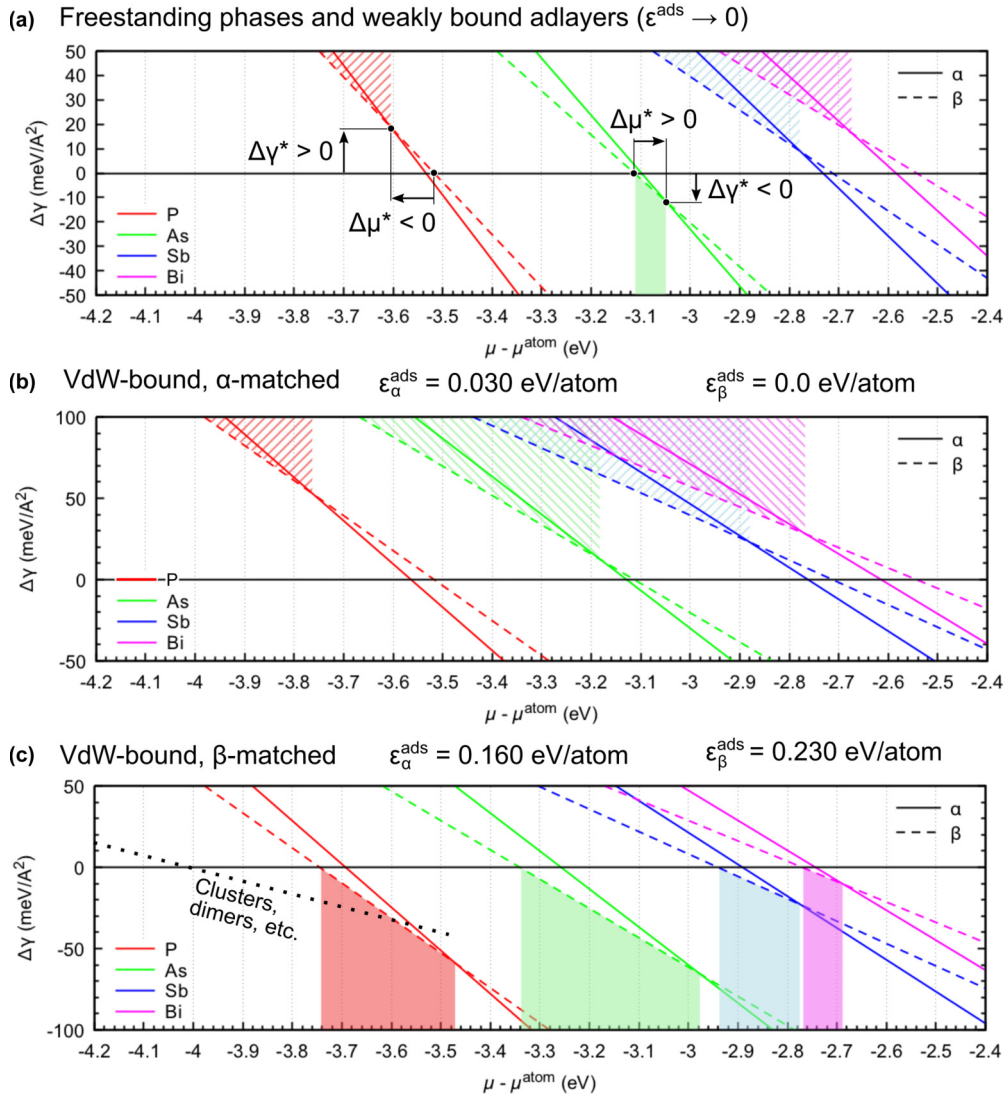


FIG. 4. Phase diagrams of α and β phase formation during a gaseous deposition process. Shaded areas below the x axis indicate where the β phase is stable, i.e., $\Delta\gamma_\beta < \Delta\gamma_\alpha$ and $\Delta\gamma_\beta < 0$; hatched areas above the x axis highlight the regions where $\Delta\gamma_\beta < \Delta\gamma_\alpha$ but $\Delta\gamma_\beta > 0$. The point $\Delta\gamma^*$ indicates the y value at the crossing between $\Delta\gamma_\beta$ and $\Delta\gamma_\alpha$, and $\Delta\mu^*$ is the x difference between this crossing point and the zero of $\Delta\gamma_\beta$. The signs of these two quantities determine the relative stability of the two phases. (a) Freestanding or weakly bound sheets ($E_{\text{ads}} \rightarrow 0$). (b) α -matched (by 30 meV) case. (c) β -matched (by 70 meV) case. A possible precursor phase is indicated for phosphorus.

this indicates that compressive lattice matching to substrates will generally discourage formation of the β phase during deposition, as a much larger adsorption energy is needed to compensate the penalty from strain.

We next consider the coupling to the substrate. The adsorption (binding) energy per atom of the sheet is defined here as:

$$\varepsilon_X^{\text{ads}} = -(E_{X/\text{sub}} - E_{\text{sub}} - E_X^{\text{FS}})/N. \quad (7)$$

In this way, $\varepsilon_X^{\text{ads}}$ implicitly includes all substrate-related interactions, including the strain penalty imposed by matching to the substrate, energy gains from charge transfer or bonding/nonbonding interactions, geometrical factors like stacking angle and position, adlayer periodicity, and so on; its value for a specific 2D layer/substrate configuration must be computed explicitly. To simplify the analysis, we hereon assume that area of the adsorbed phase remains that of the

freestanding phase (thus, slopes remain constant). This is valid in the (common) case of well matched heterostructures (see below) or for very weakly bound or incommensurate phases; otherwise one should keep in mind Fig. 5 or consider Eq. (4) directly. The formation energy can thus be expressed in terms of the adsorption energy:

$$\Delta\gamma = (E_X^{\text{FS}} - N\varepsilon_X^{\text{ads}} - \mu N)/A \quad (8)$$

and the height of the α , β crossing point becomes

$$\begin{aligned} \Delta\gamma^* &= \frac{E_\alpha^{\text{FS}} - E_\beta^{\text{FS}}}{A_\alpha - A_\beta} - \frac{N(\varepsilon_\alpha^{\text{ads}} - \varepsilon_\beta^{\text{ads}})}{A_\alpha - A_\beta} \\ &= \Delta\gamma^{\text{FS}} + \Delta\gamma^{\text{ads}}. \end{aligned} \quad (9)$$

An important consequence of Eq. (9) is that if ε_{ads} is the same for the two phases, then the sign of $\Delta\gamma^*$ cannot change with respect to the freestanding case, even in the case of

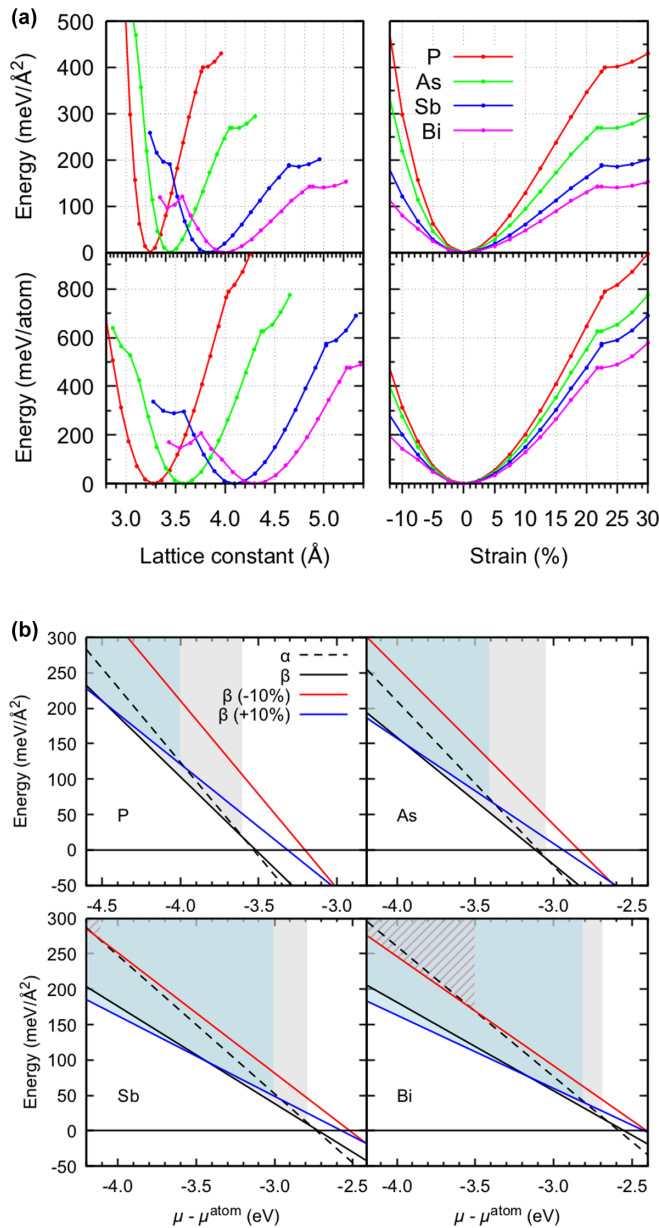


FIG. 5. (a) Total energy per area and per atom of the β phase as a function of lattice constant (left) and strain (right) for the indicated monolayer pnictogens. The (engineering) strain is defined as $(a - a_0)/a_0$; positive (negative) values indicate tensile (compressive) strain. Change in slope at high strain indicates preference for a completely flat honeycomb phase. Energies are plotted relative to the minimum in each case. Data are computed using the DF2-B86R functional. (b) Phase diagrams of freestanding α and β monolayers, and β sheets under compressive (red, -10%) and tensile (blue, $+10\%$) strain.

strong adsorption to the substrate. As Fig. 4(b) shows, a small value of $\varepsilon_{\alpha}^{\text{ads}} = 30$ meV/atom through preferential matching of the α phase is enough to make it the clearly favoured phase for all pnictogens and values of μ . Similarly, the formation of the β phase becomes generally possible through a relative increase in $\varepsilon_{\beta}^{\text{ads}}$ of 70 meV/atom. Precisely, the values of $\Delta\varepsilon_{\alpha\beta}^{\text{ads}} = \varepsilon_{\beta}^{\text{ads}} - \varepsilon_{\alpha}^{\text{ads}}$ that are needed to change the

sign of $\Delta\gamma^*$ for P, Sb, and Bi are 17, 19, and 42 meV/atom, respectively. As demonstrated in Fig. 4(c), favoring the β phase (e.g., via lattice matching) induces a dramatic change in $\Delta\gamma^*$ and $\Delta\mu^*$ with respect to that of the freestanding case. The relatively narrow range of $\Delta\mu^*$ for bismuthene, however, suggests that formation of monolayer β -Bi is limited to the cases of strong substrate interaction and perfect lattice matching.

Numerous DFT calculations of 2D pnictogen layers on metallic and nonmetallic substrates have now been reported in the literature. Formation or adsorption energy differences ($\Delta\varepsilon_{\alpha\beta}^{\text{ads}}$) have largely been given for phosphorene [33–35,47,65] allowing possible formation of a β adlayer (blue phosphorene) to be investigated from Eq. (9) and Fig. 4. Zeng *et al.* [34] studied phosphorene adsorption on several substrates with hexagonal surface cells [Au(111), Cu(111), and wurtzite BAs(001), BP(001), GaN(001)]. Within DF2-B86R, $\Delta\varepsilon_{\alpha\beta}^{\text{ads}} < 40$ meV/atom for all substrates except for Cu(111) [140 meV/atom], indicating only the latter is conducive to β -P growth (Gao *et al.* [65] demonstrated that the strong overall interaction with Cu(111) kinetically hinders formation of α -P, making it anyway a problematic substrate). Calculations by Han *et al.* [35] (PBE-D3) for phosphorene on Al(111) and Ag(111) yielded $\Delta\varepsilon_{\alpha\beta}^{\text{ads}} = 4$ and 37 meV/atom, respectively, indicating their unsuitability for forming β -P during deposition. Instead, β -P on Au(111) should be viable, with values of $\Delta\varepsilon_{\alpha\beta}^{\text{ads}}$ reported as large as 120 meV/atom [33–35,47]. Finally, Qiu *et al.* [33] using PBE-D3 reported β -P is strongly favored (by 170–232 meV/atom) on Ru(0001) and on (111) surfaces of Cu, Ni, and Pt. The moderate interfacial interactions may be weak enough to preserve the properties of the 2D material but preclude the possibility of exfoliation. On Ag(111) they reported a weaker value of 92 meV/atom. Instead, the tetragonal β -Sn(100) surface disfavours formation of β -P completely ($\Delta\varepsilon_{\alpha\beta}^{\text{ads}} = 6$ meV/atom) due to the lack of any lattice matching.

The aforementioned systems offer weak-to-moderate strain conditions. It is interesting to compare this situation with a highly strained regime that may lead to flat layers. Figure 6 shows the phase diagrams for Sb-ene formation on Bi₂Se₃ and Ag(111), respectively. For the former we took values of $\varepsilon_X^{\text{ads}}$ from Ref. [27] (neglecting SOC) and applied Eq. (9). For the latter we performed explicit DFT calculations (DF2-B86R functional) using the stable geometry for β -Sb/Ag(111) reported in Ref. [66]. Here we adopted a Ag(111)- $\sqrt{3} \times \sqrt{3}$ cell, a five-layer-thick slab, and an $8 \times 8 \times 1$ k -point mesh. An incommensurate α -phase was modelled using a larger 390 atom Ag supercell with an Sb layer (116 atoms) relaxed on top, and Γ -point sampling. This cell imparts a low strain of 0.6% on the α layer. The Sb/Ag(111) phase diagram was then generated by applying Eq. (4) directly.

Bi₂Se₃ offers a near-perfect lattice match with β -Sb, yielding negligible strain and $\Delta\varepsilon_{\alpha\beta}^{\text{ads}} = 54$ meV/atom [see also Fig. 4(c)]. As shown in Fig 6(a), this is sufficient to favor some formation of β -Sb in a narrow range of μ . The value $\varepsilon_{\beta}^{\text{ads}} = 192$ meV/atom is moderate, reflecting ordered vdW heterostructure growth. Instead, the larger lattice constant in Ag(111) implies that a highly strained (22%) monolayer must form to fulfill a perfect (1 \times 1) registry. The strain penalty (582 meV/atom) in this case is substantial, as can be seen by

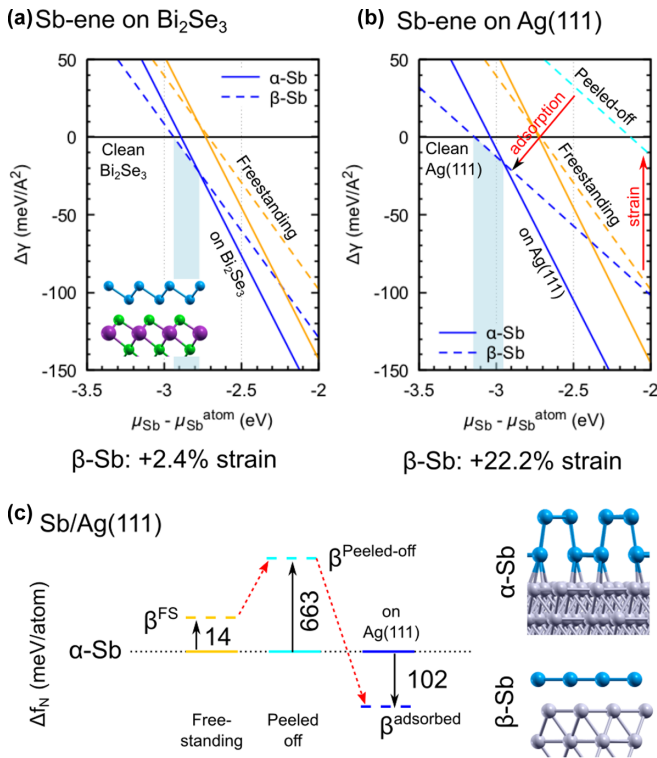


FIG. 6. Phase diagram describing epitaxial formation of α -Sb (solid lines) and β -Sb (dashed lines) on (a) Bi_2Se_3 (data taken from Ref. [27]) and (b) $\text{Ag}(111)$. (c) Relative formation energies per atom for freestanding, peeled-off, and adsorbed Sb-ene on $\text{Ag}(111)$.

comparing the freestanding (FS) and peeled-off (i.e., the 2D layer in its adsorbed geometry) lines in Fig. 6(b). Nonetheless, this is compensated by a strong interaction with $\text{Ag}(111)$ which leads to $\Delta\varepsilon_{\alpha\beta}^{\text{ads}} = 90$ meV/atom and, indeed, possible formation of β -Sb on this substrate. Note that the large adsorption energy (~ 1.0 eV/atom) of the peeled-off β sheet for this phase suggests chemisorption. This contradicts the authors' reports of a weak antimonene-silver interaction [66]. We investigate the nature of the interaction in more detail in the Appendix.

In short, during a deposition process the α phase monolayer pnictogen is favored to form simply due to its higher density of atoms per area. The β allotrope may become stable for particular values of chemical potential if its adsorption energy is relatively large (≥ 50 meV/atom) compared to that of the α phase. Typically this requires some lattice matching with low tensile strain; however larger tensile strain may in some cases be compensated by strong interfacial bonding, while compressive strain strongly discourages the formation of the β phase.

IV. STABILITY UNDER ANNEALING CONDITIONS

If the gaseous reservoir is not present or is removed during a subsequent annealing stage, the thermodynamical boundary conditions are modified. The number of atoms N is now limited, being supplied solely by the deposited adlayer, and the area A is a free parameter. The stability of a given phase is then determined by the formation energy *per atom* f_N , given by

$f_N = (U - TS)/N$. As before, we neglect the entropy term, and thus f_N depends only on the total energies. Expressing this in terms of the adsorption energy of the sheet yields

$$\Delta f_N = (E_X^{\text{FS}} - N\varepsilon_X^{\text{ads}})/N. \quad (10)$$

Relative stabilities can thus be deduced from the relative cohesive energies of the freestanding phases ($\Delta\varepsilon_{\alpha\beta}^{\text{coh}}$, see Fig. 2) and relative adsorption energies $\Delta\varepsilon_{\alpha\beta}^{\text{ads}}$ (including strain).

Thermal annealing is typically useful to transform a metastable disordered phase formed during the deposition phase, such as one composed of local islands, clusters, chains, etc. [see dotted line in a Fig. 4(c)], into a stable crystalline phase. In the current context, this metastable phase may already consist of a complete 2D pnictogen monolayer, or a mixture of allotropes, as determined by the phase diagram and particular growth conditions during deposition. A gentle annealing procedure may thus induce a transformation of the deposited phase into the most stable allotrope. Whether the transformation will proceed [27] or remain trapped in the metastable state [47] depends on the barrier height, which is analyzed in the following section.

A. Phase transition pathways

In the previous section we saw that the α and β phases (the latter under certain conditions) are the most favoured allotropes formed during a deposition process. We therefore focus on transformations between these two phases by means of a systematic study. Calculations of the pathway and barrier height have previously been reported for P [26,47], As [67], Sb [27,28,68], and Bi [29]. However, the methodologies used (choice of code, NEB approach, and XC/vdW potential) generally differ, thus leading to a wide variety of results (see below). This makes it impossible to identify trends and interpret common features in the data. Transformations among some other pnictogen phases (including green phosphorene) have been studied elsewhere [44,67]. Furthermore, Zhou *et al.* [69] reported an $\alpha \rightarrow \beta$ transformation in the nonpnictogen 2D material stanene grown on a $\text{Au}_2\text{Sn}(111)$ alloy. We were unable, however, to stabilize the washboard geometry of the freestanding α phase using Sn. Note that the process discussed here is not to be confused with the thickness-dependent $\alpha \rightarrow \beta$ phase transformations well known in bismuthene [70,71] and recently reported in antimonene [72].

Computed transition pathways for the four pnictogens are reported in Fig. 7. The optimal bond-breaking (BBP) and bond-flipping (BFP) pathways, introduced in Sec. II C, are shown in each case. Bond-flipping pathways are very similar for all four species. The pathway itself is almost symmetric with two transition states (T1 and T2) very close in energy. As noted above, the BFP represents a displacive phase transition involving flipping or rotation of one bond per simulation cell containing four atoms. In each transition state, the atoms in the flipping bond move into an sp^2 -like geometry.

The bond-breaking path is instead a reconstructive transition. Its profile is qualitatively similar for the four pnictogens, being asymmetric with three peaks (A, B, and C) that gradually decrease in energy as we move down the periodic table. However, there are some important differences. While the largest peak for P-ene occurs midway through at B, the

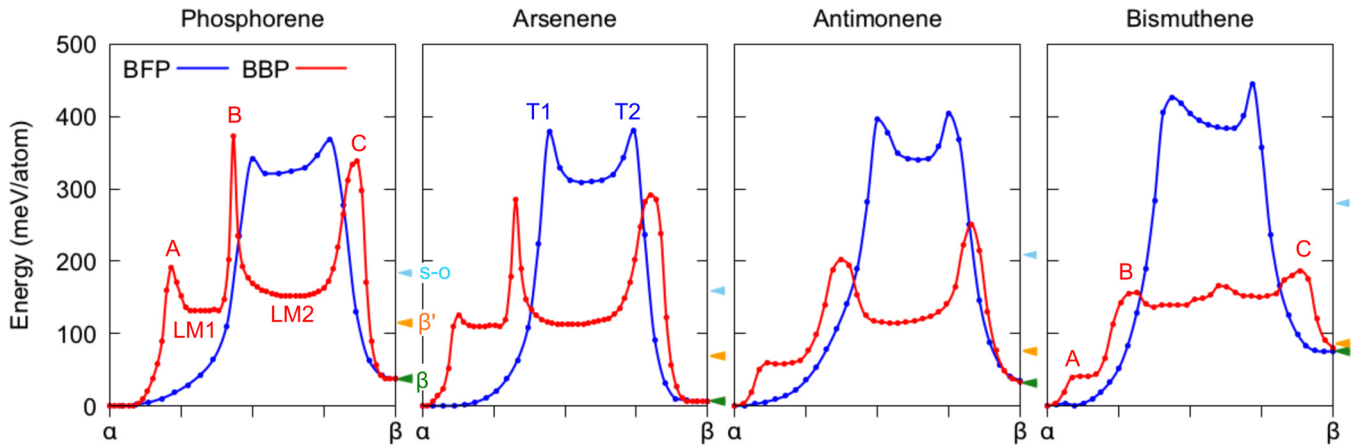


FIG. 7. Minimum energy pathways between α and β phases computed with PBE-D2. Bond-flipping paths (BFP) and bond-breaking paths (BBP) are shown. Transition states common to all elements are labeled. Triangles on the side of each panel indicate the energy of the β , β' , and s - o phases relative to the α phase.

maximum barrier instead switches to the final peak C for the other elements, which decays less quickly than B. In Bi-ene, the peaked structure is hard to distinguish: In fact, it is quite difficult to identify a well-defined MEP in this case, reflecting the ability of Bi to assume multiple coordinations.

The BFP and BBP thus have fundamentally different line-shapes. In the BFP case, the two transition states (T1,T2) are separated by a shallow local minimum, whose geometry is simply an intermediate between the two sp^2 -like states. Instead, in BBP simulations the system is free to locate deeper local minima that correspond to metastable structures that do not conserve the hexagonal geometry common to α and β phases. Two distinct local minima geometries are observed for the four systems. The first (LM1) corresponds to a 2D phase [73] predicted from exfoliation of a high pressure phase of bulk Sb [74]. The second (LM2), previously noted in Ref. [27], resembles the proposed η phase of antimonene [3]. Like the s - o phase it is composed of a lattice of octagons and squares, however the ordering of atoms in the upper and lower layer is different. Moreover the relative energy of the s - o phase is anyway higher than the LM2 energy, as indicated on the right of each panel in Fig. 7, making it unlikely to form through thermal annealing. Nonetheless, thermal annealing from the α phase might lead to formation of *novel* 2D phases if the interaction with the lattice can be tuned to their favor, e.g., as noted above for the green-P phase.

B. Transition barriers

The heights of the $\alpha \rightarrow \beta$ transition barriers for each element and pathway are compared in Fig. 8(a) for the PBE-D2 and DF2-B86R functionals, respectively. For the sake of simplicity, we consider the forward barrier from α to β . While the bond-flipping path barriers increase (or slightly decrease, for DF2-B86R) for heavier elements, the bond-breaking path shows a consistent decrease in barrier height from left to right. As a result, within PBE-D2, the BBP barrier for bismuthene is actually less than half of its BFP counterpart. On the whole, the BBP is the more favored pathway. Barrier heights for phosphorene have roughly the same value irrespective of the

pathway or functional, although PBE-D2 actually predicts the BFP becomes slightly more favored for this element.

The absolute value of the barrier height is the key quantity that decides whether the phase transformation can take

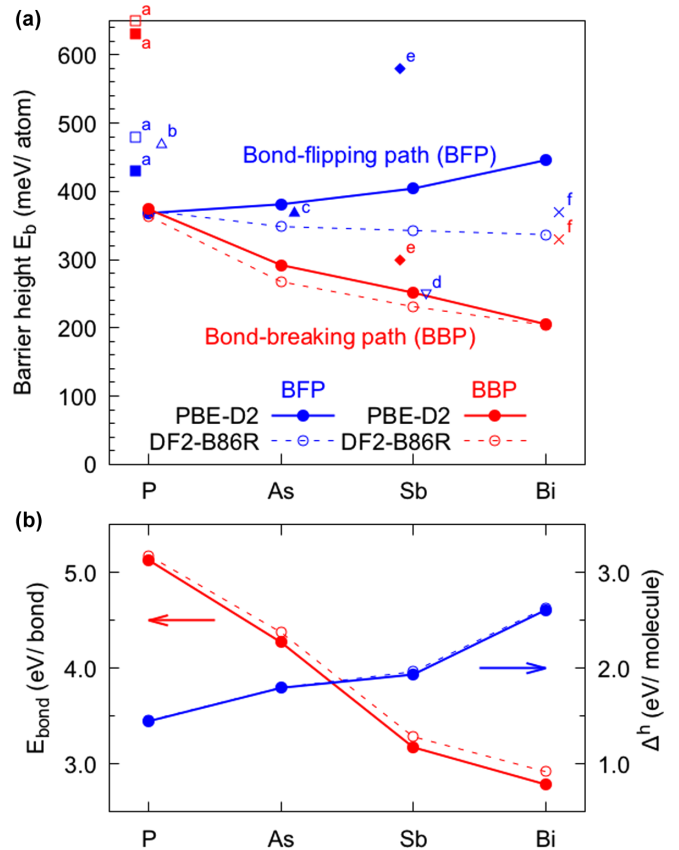


FIG. 8. (a) Trends in barrier height for the $\alpha \rightarrow \beta$ forward phase transition, computed with PBE-D2 and DF2-B86R. Bond-flipping path (BFP) is shown in blue; bond-breaking path (BBP) is in red. Literature data from Ref. [47]^a (solid squares: PBE, open squares: optB86b), Ref. [26]^b (PBE), Ref. [67]^c (PBE), Ref. [68]^d (PBE, doped), Ref. [28]^e (PBE), Ref. [29]^f (PBE-D2). (b) Computed bond dissociation energies (red) and ‘hybridization’ energies (blue, see text).

place under thermal annealing. The origin of the barrier in the two pathways is quite different. In the case of bond-breaking paths, each barrier corresponds to changes in atomic coordination via breaking of bonds. In fact, all four atoms in the simulation cell experience a simultaneous bond breaking/rebonding at *every* barrier for the three lighter pnictogens. The clear trend of lower barrier height with atomic number is strongly correlated with the bond dissociation energy E_{bond} as demonstrated in Fig. 8(b) (red lines). Here E_{bond} is defined as the energy to dissociate a pnictogen dimer into its atomic constituents (including spin polarization). As the pnictogen character moves from insulating to metallic, the upper and lower atomic planes of the 2D allotrope are able to move more freely and thus find a lower energy pathway more directly. In the case of bismuthene, the barriers themselves are not clearly distinguished, and distinct bond-breaking events are hard to identify. Nonetheless it follows the trends in barrier height and bond dissociation energy, suggesting the simple model holds true also for bismuthene.

In the BFP case, a possible reason for the barriers is the local formation of a flat sp^2 -like geometry around the atoms undergoing a ‘flip,’ without any change in atomic connectivity. We investigated this hypothesis by computing the energy difference Δ^h between a trigonal pyramidal and a trigonal planar Pn-H₃ molecule (Pn = pnictogen). Trigonal pyramidal Pn-H₃ molecules are well known to comprise an almost pure s -character lone pair and three unhybridized pnictogen p orbitals [75], as attested by the computed bond angles which range from 92.6° (PH₃) to 90.1° (BiH₃). The nearly ideal 90° angles found in the heavier elements is a manifestation of the inert lone pair effect. The similar angles found in the β phase pnictogens (from 92.5° in β -P to 90.3° in β -Bi) indicate a similar orbital character and suggest the Pn-H₃ molecules capture the local chemistry in the 2D system. We note that a study of the bond character in α -P using maximally localized Wannier functions found that the in-plane bonds (zigzag chains, bond angle of 93.5°) are formed from essentially unhybridized p_x and p_y orbitals; these mix partially with the p_z and s orbitals to form two hybrid orbitals bent along the a_1 direction that form the interlayer bond (bond angle of 103.5°) and lone pair, respectively [76]. Our computed in-plane bond angles of 95.8°–93.6° in the α -phase pnictogens also indicate unhybridized p -orbital character. The asymmetric washboard geometry adopted by Sb-ene and Bi-ene further allows two atoms per cell to adopt an almost pure p character with three orthogonal p orbitals used for bonding and the remaining s orbital hosting the lone pair. This unhybridized or weakly mixed s - p character thus dominates both α and β phases of 2D pnictogens, especially from As downwards [75], in contrast to some claims in the literature of sp^3 hybridization (ideal angle 109.5°).

A trigonal planar geometry in the Pn-H₃ molecule or an sp^2 -like geometry at the BFP transition state thus imposes either an unfavoured orbital hybridization or significant orbital strain on the pnictogen atom. Our computed values for Δ^h are plotted in Fig. 8(b) (blue lines) and can be compared with the BFP barrier heights E_b in Fig. 8(a). While the simple molecular model explains well the P-ene data ($\Delta^h = 1.45$ eV/molecule $\sim E_b = 1.48$ eV/cell), it is less successful at explaining the data for heavier pnictogens and

even shows an opposite trend with respect to the BFP results computed using the DF2-B86R functional. This weak correlation may be explained by the observed deviation from a symmetric sp^2 -like geometry in the transition state of the larger pnictogens (one bond angle tends to remain at $\sim 90^\circ$ and one bond length differs from the others), which have a much stronger tendency to retain unhybridized s and p orbitals where possible.

The bond-flipping pathway has been investigated before in the case of phosphorene [26,47], arsenene [67], antimonene [27,28,68], and recently bismuthene [29]. One possible bond-breaking pathway was also suggested for phosphorene [47], antimonene [28], and bismuthene [29]. The various reported barriers are plotted in Fig. 8 as distinct data points. For phosphorene, there is a wide range of data available. Tristant *et al.* [47] reported barriers of 430–480 meV for the bond-flipping paths, significantly lower than those of their investigated BBP path (640–650 meV). We do not find such a large difference between the two pathway barriers in phosphorene, and our computed barrier of about 375 meV is considerably lower than their data by 100–250 meV. In an earlier study, Zhu *et al.* [26] reported a higher BFP height of 470 meV in phosphorene using PBE. Concerning arsenene, the reported value (which neglects vdW) is actually very close to our data for the same BFP path. A low barrier of 250 meV for the BFP pathway in hole-doped antimonene was reported in Ref. [68]. More recently, BFP and BBP pathways were reported by Shi *et al.* [28] for antimonene using PBE without vdW and by Zhou *et al.* [29] for bismuthene within PBE-D2.

The wide discrepancies between the reported data and our calculations stem from different (or lack of) vdW interactions as well as the higher precision obtained in our vNEB calculations. In particular, our simulations use far more images (30–50 versus, in some cases, 4–5), allow the simulation cell geometry (both lattice constants and angles) to distort along with the atomic displacements, utilize climbing and downing images, and consider many possible bond-breaking pathways. When few intermediate images are used it is likely that the transition state is missed.

Our calculations therefore predict considerably lower barriers than those reported previously, and yield consistent trends as heavier elements are used. If only DF2-B86R results are considered, the BBP represents the true MEP for all four pnictogens. (The BFP might be clearly favored in the case of another pnictogen, nitrogene, due to its higher bond dissociation energy and possibility to undergo sp^2 hybridization.) Future simulations utilizing the (simpler) BFP should therefore be avoided.

Finally, we comment on the impact of the substrate on the $\alpha \rightarrow \beta$ phase transformation (see Ref. [27] for a quantitative discussion). Since the adlayer unit cell changes size and symmetry during the transformation, it is not technically feasible to simulate the process if periodic boundary conditions are assumed. Nonetheless, since lattice matching is anyway not favored along most of the pathway, it is reasonable to assume an incommensurate adlayer at the saddle points. Thus the barrier height should remain unchanged with respect to the incommensurate initial (or final) stage. Instead, we expect that lattice matching will drive the direction of the transformation towards the lower energy (lattice matched) phase. Charge

transfer to or from the adlayer may also play a role. We tested the effect of hole doping [68] on the BFP path in antimonene and found only a negligible effect on the pathway and barrier height. The role of the substrate in these simulations thus deserves further study; a molecular dynamics study may be insightful.

V. DISCUSSION

In the previous sections we have presented strategies for understanding and predicting epitaxial growth of pnictogen monolayers based on simple thermodynamical arguments. In order to achieve this, we provided a rigorous first principles study of pnictogen stability and phase transformations which give rise to various physical and methodological insights. Before we discuss these results in the context of reported experimental results, we first summarize the key methodological and physical points.

Our study of cohesive energies in freestanding pnictogens (Sec. II B) confirms that the α phase is the most stable for P, Sb, and Bi, while the β is stable for As. Inclusion of vdW interactions is crucial; DF2-B86R appears to give consistent results. Spin-orbit coupling has little effect on relative cohesive energies. We consider the ‘green’ allotrope to be a straightforward 1:1 blend of α and β phases; many other such mixed allotropes are, in theory, possible. Other phases are clearly less stable and therefore not investigated further. The ‘MBi’ phase proposed to explain STM observations in Ref. [41] is ~ 250 meV/atom less stable than α -Bi, indicating a uniquely strong interaction with the substrate, or a deficiency in the model. The energy difference between the α and β phases is quite small (from -42 to $+15$ meV/atom). They form the basis of the phase diagrams describing epitaxial growth.

During a gaseous deposition process, the adlayer growth is described by the formation energy *per unit area*, which only depends on the relative cohesive and adsorption energies and the surface atom density. Single α monolayer formation is favored, especially at higher chemical potential μ , as it maximizes the adlayer surface density. Nonetheless, the β phase can be induced if its adsorption energy is higher than the α phase by at least 20–40 meV/atom. This can typically be achieved via favorable lattice matching and low strain, conditions more easily achieved in Sb and Bi. Tensile strain enhances the preferability of the β phase for small μ because it increases the difference between the adlayer densities of the two phases. Highly-strained flat geometries are feasible in the case of strong pnictogen-substrate interactions, not necessarily purely covalent.

In the absence of a gaseous reservoir, such as during an annealing process, the formation energy *per atom* of the heterostructure determines the most stable adlayer geometry. Kinetic barriers may however prevent transformation from the adsorbed phase. Careful simulations of phase transitions between the stable α and β phases reveal that a reconstructive transformation—the bond-breaking path—is most favored for all pnictogens. BBP simulations are sensitive to computational parameters which may explain the wide variation in published data. The trend in the barrier height for heavier pnictogens simply follows the trend of lower bond dissociation energy.

Other allotropes may be formed locally during the process, and may be engineered if an appropriate substrate is used. Our results show that thermal annealing is a viable route towards controlled synthesis of particular allotropes of all 2D pnictogens.

A. Experimental synthesis via deposition

Table II lists some key reports of 2D monolayer pnictogen synthesis on a variety of substrates through deposition without annealing. Epitaxial monolayer growth of P-ene and As-ene have rarely been achieved, in contrast to Bi-ene and especially Sb-ene. (Earlier reports of phosphorene growth appear to be 2D Au-P alloys [3,77,78]). It is immediately clear that there is a strong tendency for the grown monolayer phase to match symmetry with that of the substrate [i.e., β on hexagonal (h) or α on rectangular (r) surface unit cell]. Nonetheless it is important to note that growth of either phase may be theoretically possible during deposition if μ is tuned appropriately.

In the case of β phase growth, a moderate interfacial interaction pushes $\Delta\varepsilon_{\alpha\beta}^{\text{ads}} > 40$ meV/atom and thus opens a range of chemical potential $\Delta\mu^*$ that favors its formation. As seen previously, this is most favored in the case of low, tensile (positive) strain. The recent report of β -P synthesis on Au(111) thus supports the predictions made in Sec. III based solely on $\Delta\varepsilon_{\alpha\beta}^{\text{ads}} = 120$ meV/atom. However, very large strain can also be accommodated if a strong enough interaction with the substrate is found. For instance, in the β -Bi/SiC case the mechanism for stabilization is reported to occur via bonding to p_z orbitals of the overlayer following rehybridization to an sp^2 character. For β -Sb on Ag(111), our calculations shown in Fig. 6(b) demonstrate that a strong interaction compensates for the large strain penalty of -582 meV/atom, also overcoming the considerable adsorption energy (~ 340 meV) of the quasi-incommensurate α -Sb phase. However, the β phase remains favored only in a narrow range of chemical potential (Fig. 6). This explains why, like for Sb on Bi₂Se₃, only small islands or domains of β phase appear without annealing [64]. Other mechanisms may also drive stability. Spin-orbit coupling is important for Sb/Bi₂Se₃ due to the hybridization of Sb states with topological surface states of the substrate and topologization of the adlayer [79,80]. Moreover, the formation of quasifreestanding β -Sb on thin Pb(111) films is driven via hybridization of Sb with one-dimensional Pb quantum size effect states [81].

For the case of α phase formation, there are two possible routes to synthesis. Following the discussion in Sec. III, the α phase can always be favored if a high enough value of μ is set experimentally, e.g., by increasing the coverage/flux or (typically) via low temperatures. This was demonstrated, for instance, on Bi₂Se₃ even though the β -Sb phase is well matched to the substrate [see Fig. 6(a)] [27]. Alternatively, use of a rectangular lattice to disfavor β formation can be enough to keep $\Delta\gamma^* > 0$, although clearly some lattice matching will strongly favor an α phase formation (see, e.g., α -Sb on T_d-WTe₂ [82] and on SnSe [83]). We note that the (biaxial) strain reported for α phase layers is typically less than 5% and is not necessarily tensile. Slight changes in flux or temperature can lead to formation of both phases. For instance, while formation of β -Sb was reported on an α -Bi substrate, adding

TABLE II. Summary of key experimental reports of direct epitaxial growth (without annealing) of 2D pnictogen (Pn) monolayers. The hexagonal (h) or rectangular (r) symmetry of the adlayer and surface is indicated, following Le Ster *et al.* [89] ‘Perfect’ registry indicates (1×1) on (1×1) commensurate epitaxial match, and includes highly strained, flat overlayers; ‘Good’ indicates a coincidence lattice (the adlayer periodicity is reported); ‘Weak registry’ indicates an incoherent lattice or quasi-freestanding overlayers. Strain of α (a_1, a_2) and β (a) components, defined as $(a^{\text{exp}} - a^{\text{calc}})/a^{\text{calc}}$, using the DF2-B86R lattice parameters (Table I).

Pn	Phase	Substrate	Stacking symmetry	Lattice registry and adlayer periodicity	Strain (%)		Reference
					$\alpha(a_1, a_2)$	$\beta(a)$	
P	β	Au(111) silicide	h/h	good (5×5)		+5.4	Zhang <i>et al.</i> [23]
As	β	Ag(111)	h/h	good (4×4)		+0.9	Shah <i>et al.</i> [25]
Sb	α	T_d -WTe ₂	r/r	good ($\sqrt{2} \times \sqrt{2}$)	(+1.8, +1.4)		Shi <i>et al.</i> [82]
Sb	α	α -Bi/MoS ₂	r/r	weak registry	(+3.1, -1.2)		Märkl <i>et al.</i> [84], Le Ster <i>et al.</i> [89]
	β		h/r	weak registry		-1.5	
Sb	α	SnSe	r/r	perfect (1×1)	(+1.0, -1.2)		Shi <i>et al.</i> [28]
	β		h/r	weak registry			Shi <i>et al.</i> [83]
Sb	α	Bi ₂ Se ₃	r/h	weak registry	(+1.8, -0.9)		Hogan <i>et al.</i> [27]
	β		h/h	perfect (1×1)		+2.4	Flammini <i>et al.</i> [64], Hogan <i>et al.</i> [27]
Sb	β	PdTe ₂	h/h	perfect (1×1)		+0.7	Wu <i>et al.</i> [90]
Sb	β	Sb ₂ Te ₃	h/h	perfect (1×1)		+4.0	Lei <i>et al.</i> [91]
Sb	β	Bi ₂ Te ₃	h/h	perfect (1×1)		+7.0	Lei <i>et al.</i> [91]
Sb	β	SbAg ₂	h/h	good (2×2)		+5.7	Sun <i>et al.</i> [92]
Sb	β	Pb(111) films	h/h	good (6×6)		-0.2	Jatochowski <i>et al.</i> [81]
Sb	β	Cu(111)	h/h	perfect (1×1)		+8.1	Zhu <i>et al.</i> [61]
Sb	β	Ag(111)	h/h	perfect (1×1)		+22.2	Shao <i>et al.</i> [66]
Bi	α	HOPG	r/h	weak registry	(-0.2, -3.1)		Lu <i>et al.</i> [93]
Bi	α	HOPG	r/h	weak registry	(+0.1, -0.9)		Kowalczyk <i>et al.</i> [94]
Bi	β	Bi ₂ Te ₃	h/h	perfect (1×1)		+2.0	Yang <i>et al.</i> [95]
Bi	β	Bi ₂ Te ₂ Se	h/h	perfect (1×1)		+1.5	Kim <i>et al.</i> [96]
Bi	β	SiC	h/h	good (1×1)		+24.6	Reis <i>et al.</i> [97]

more Sb results in a restructuring of the layer into the α phase [84]. Mixed phases were also reported on SnSe [28] and on Bi₂Se₃ [64], consistent with a narrow range of $\Delta\mu^*$. In fact, it is more typical to grow complete islands that are 100% formed by α -Sb [27,28].

B. Experimental synthesis via annealing

The experimentally observed phase after an annealing stage should simply correspond to the most stable phase as defined by the formation energy per atom given by Eq. (10). Some key examples of monolayer pnictogens prepared in this way include flat β -P grown on Cu₃O₂ [24]; β -Sb on Ge(111) [32]; β -Sb prepared on both hexagonal Sb-Cu(111) and rectangular Sb-Cu(110) surface alloys [85]; and β -Sb, α -Bi, and β -Bi on Cu₃O₂/Cu(111) [29,86]. In most of these cases initial deposition results in a phase high in disorder or composed of pnictogen precursors such as aggregates, dimers or chains [87]; annealing allows the system to escape from these metastable states and find a more stable (or global) minimum. It is notable that, with the exception of Ge(111), all these synthesized pnictogen layers appear to experience moderate strain (5–8%). For P/Cu₃O₂, the phosphorene sheet exhibits corrugations (consistent with the observed Moiré pattern) that relieve strain as well as presence of regular covalent P-O bonds [24].

We now return to the alternative scenario for synthesis by means of annealing-induced phase transformations between α and β phases. The barrier heights determine the probability for a transformation to occur in real experiments, which has

important implications for interpreting measurements as well as controlling synthesis of a particular allotrope. Previously it was suggested that a barrier in P-ene of 0.47 eV/atom was low enough to enable mechanical conversion [26] but high enough to remain kinetically unlikely [47]. Our calculations (Fig. 8) of the barrier heights are consistently lower however than the literature values and range from 363 meV/atom in P-ene to 204 meV/atom in Bi-ene. Within a simple Arrhenius picture of the transition, the reaction rate constant for the four-atom cell is given by $Ae^{-4E_b/kT}$, where E_b is the barrier height or activation energy per atom, and A is the pre-exponential frequency factor. Although the precise value of A is undetermined, a rapid $\alpha \rightarrow \beta$ transformation has been observed experimentally for Sb-ene on Bi₂Se₃ [27] at 473 K and for Bi-ene on Cu₃O₂/Cu(111) at 500 K [29]. The slightly higher computed barrier for As-ene thus suggests that the $\alpha \rightarrow \beta$ transformation may well be accessible at typical annealing temperatures of 350–550 K also in this material; the transition in P-ene remains relatively unlikely. One should bear in mind however that these barriers are likely to be upper limits to the true ones, as in addition to the nucleation-propagation phenomenon discussed earlier, they can further be modified by vibrational contributions to the free energy [47], domain walls, other kinetic effects, and the impact of the substrate (charge doping and preferential matching of one phase) [27]. For instance, a reduction of 13% in barrier height due to nucleation increases the rate constant in P-ene by a factor of about 75. A careful temperature-controlled STM study of the $\alpha \rightarrow \beta$ transition in one well characterized pnictogen system as a function of annealing temperature would

provide validation of the theoretical predictions and transition paths.

An opposite phase transformation, from a (distorted) β phase to the α phase, has been reported recently on SnSe [28]. The α phase forms directly during antimony deposition at 400 K, and in spite of the rectangular cell of the substrate surface, is reported to be quasifreestanding [83]. Instead, if the surface is prepared at 350 K, a mixture of the two phases appears, and post-annealing at the same temperature induces the transition to the α phase. DFT calculations indicate the adsorbed α is more stable by about 50 meV/atom, meaning $\Delta\varepsilon_{\alpha\beta}^{\text{ads}} \sim -30$ meV/atom. Under such conditions, $\Delta\gamma^*$ is positive and the β phase should not form. We therefore suggest that the formation of β -Sb regions is facilitated by the perfect lattice matching observed at the α - β phase boundary [83] and which may stabilize the observed distorted hexagonal lattice. In summary, all available experimental results and observations can be understood within the thermodynamical framework we developed, which is thus expected to predict the 2D pnictogen allotrope growth and stability on any substrate.

VI. CONCLUSIONS

Epitaxial formation of 2D pnictogen allotropes can be largely explained by thermodynamic principles describing deposition and annealing regimes. While the α phase is generally favoured due to its high atomic density, formation of the β phase is easier to control due to the wider possibility of commensurate growth under low to moderate tensile strain. Although large strain appears to rule out flat geometries *a priori*, it appears that even common metal surfaces can host highly strained layers of Sb and Bi in particular. An alternative strategy for preparing ordered layers of a particular allotrope is via thermal induction of a 2D phase transition. Our calculations show that, if nucleation-propagation processes are considered, the transition barriers are quite accessible at typical annealing temperatures for all pnictogens, in contrast to previous predictions. We suggest that *ab initio* molecular dynamics or metadynamics studies of the phase transition and the initial growth mechanisms will deepen further our understanding of these epitaxial growth processes [87,88]. The analysis presented herein will help guide experimental synthesis of quality pnictogen monolayers, while the theoretical and methodological analysis can be applied to other 2D systems.

ACKNOWLEDGMENTS

We thank CINECA for high-performance computing resources and support via the ISCRA initiative. C.H. thanks Giacomo Giorgi for valuable discussions and analysis.

APPENDIX: INTERACTION OF ANTIMONENE WITH Ag(111)

As reported in Fig. 6, β -Sb adsorbs much more strongly on the Ag(111) surface than α -Sb, in spite of the large strain experienced by the former. In the following we elucidate the

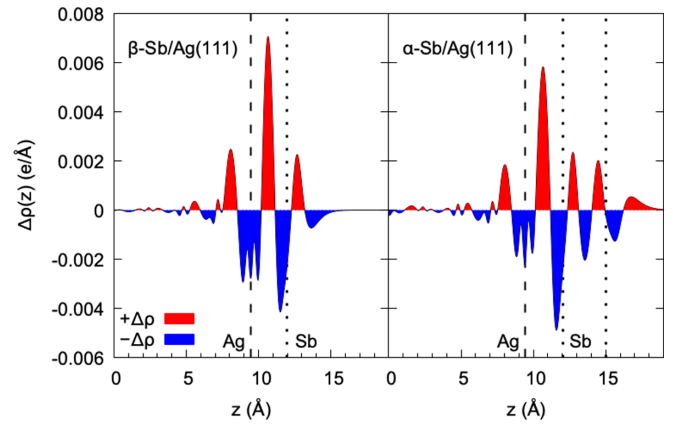


FIG. 9. Plane-averaged electron density difference perpendicular to the interface. Vertical lines indicate the positions of the Sb layer(s) and uppermost Ag atomic layer. Red indicates an accumulation of charge; blue a depletion.

main physical and chemical phenomena behind this difference.

First, using Bader analysis we identified a charge transfer from the Sb-ene to the metal surface of $0.049 e/\text{Sb}$ atom ($0.0043 e/\text{\AA}^2$) for the β phase and $0.013 e/\text{Sb}$ atom ($0.0025 e/\text{\AA}^2$) for the α phase. In other words, charge transfer is two–four times higher for the β phase and should lead to the creation of a stronger interface dipole. These values are not very large, although they appear consistent with a computed drop in work function of the Ag(111) surface following Sb adsorption (0.45 eV for β -Sb and ~ 0.02 eV for α -Sb).

The surface charge redistribution is not straightforward to interpret. Figure 9 shows the planar average of the electron density difference $\Delta\rho = \rho_{\text{Ag/Sb}} - \rho_{\text{Ag}} - \rho_{\text{Sb}}$ along the z axis perpendicular to the surface (the three terms represent the electron density for the heterostructure, Ag surface, and adsorbed Sb sheet, respectively). For both allotropes there is an accumulation of charge in the interlayer region which is slightly more pronounced in the β phase. Analysis of $\Delta\rho(\mathbf{r})$ indicates directional dipole formation along Sb-Ag bonds in this case. The Ag/ β -Sb interface also exhibits a larger charge depletion at the Ag surface. In contrast, α -Sb shows a redistribution of charge to the upper atomic Sb layer (confirmed by Bader analysis).

Further characteristics of the interfacial properties are investigated in Figs. 10 and 11. As reported by Shao *et al.* [66], flattening of the Sb monolayer is accompanied by a rehybridization of its orbitals into decoupled p_z and sp^2 -like components. This is confirmed in Fig. 10(a). On adsorption, the latter component remains mostly unperturbed by the Ag bands as shown in Fig. 10(b). Instead, the p_z orbital clearly hybridizes with several Ag bands. This indicates that for the β phase at least, there is also a chemical coupling between the two materials which should induce a measurable change in the Ag chemical environment.

Finally, in Fig. 11 we plot the electron localization function (ELF) for both interfaces. The ELFs are shown as 2D plots through vertical planes that axially cut an Sb-Sb bond close to the surface and as 1D plots along different bond axes. Plots for the incommensurate Ag/ α -Sb interface are shown for two

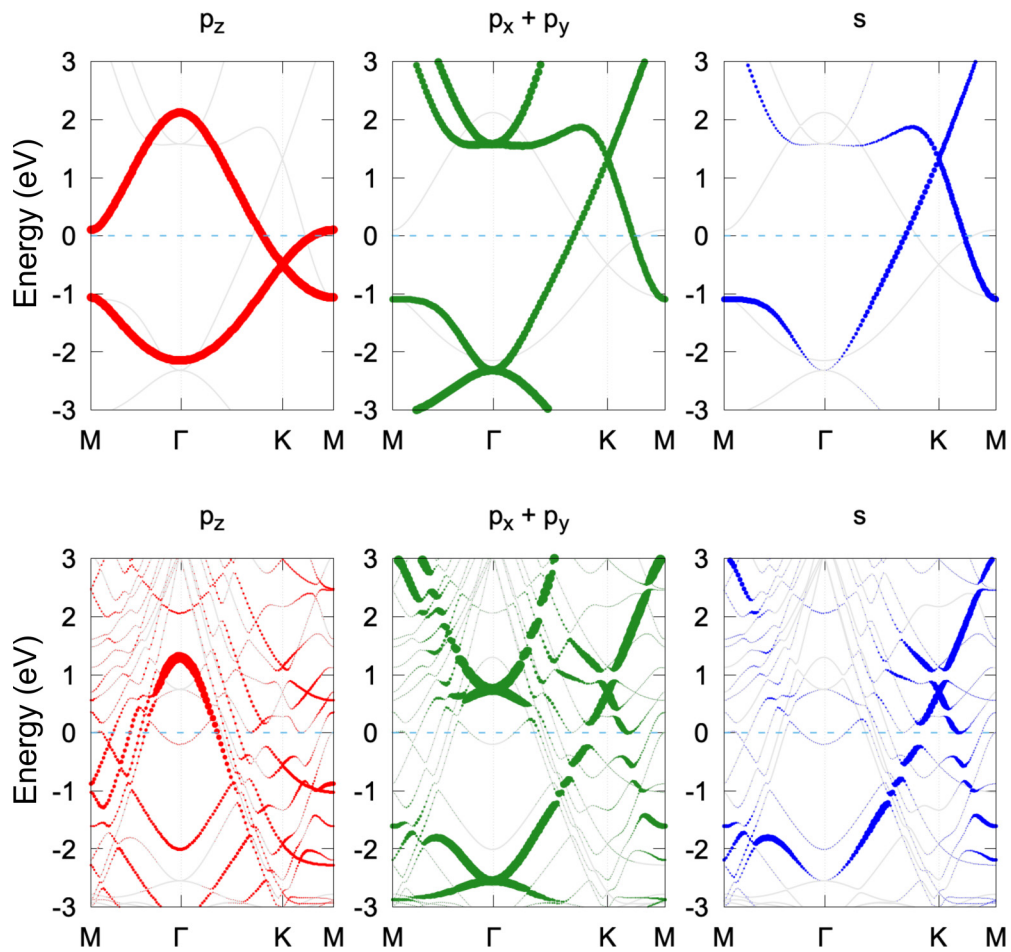


FIG. 10. Band structures of peeled-off (flat) β -Sb (top) and of the Ag(111)/ β -Sb interface (bottom). Colors indicate projections on specific Sb orbitals; spot size indicates the projection intensity (the s component is enhanced for clarity).

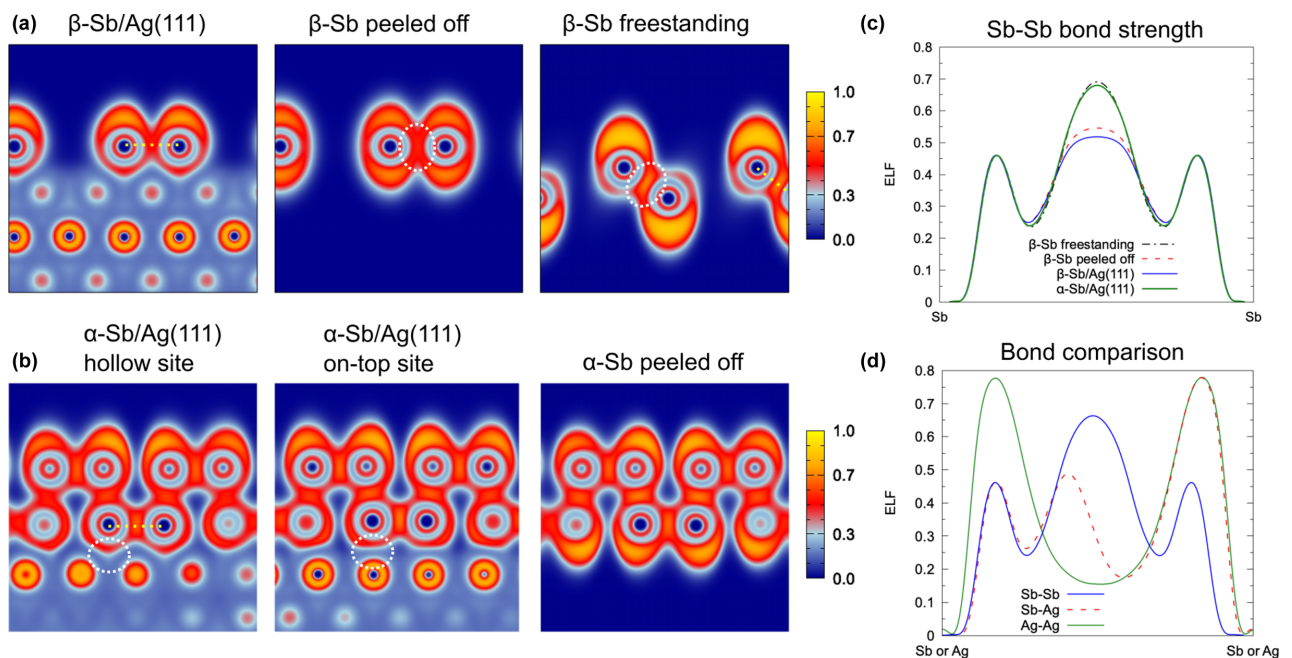


FIG. 11. Electron localization function (ELF) for isolated Sb-ene and the Ag/Sb-ene interface. (a),(b) Vertical 2D plots cutting through an Sb-Sb bond axis. Dotted circles highlight changes in the bond character. (c) 1D plots along the Sb-Sb bonds indicated by dotted lines in (a) and (b). (d) Comparison of 1D ELF plots along typical bond axes. Bond distances have been normalized to the same value for clarity.

typical sites. Flattening of the buckled β -Sb layer is found to cause a reduction in ELF between the atoms, indicating a weakening of the Sb-Sb bond. Instead, the Sb-Sb bond in α -Sb exhibits a profile like that of freestanding β -Sb, as expected. Adsorption on Ag causes changes in the lower lobe of the Sb ELF. For β -Sb and for α -Sb over a hollow site, the lobe is pinched. Over a top site, however, the lobe is largely flattened, possibly reflecting a ‘pushback’ effect due to Pauli repulsion. Figure 11(d) reports the ELF profile along typical bonds in the adsorbed systems. The Ag-Ag bond is clearly metallic (falling to 0.2 between atoms). The Sb-Sb bond is mostly covalent in nature (0.5–0.65 at midpoint). The Sb-Ag bond exhibits a

peak of 0.4–0.5 in the interatomic region. This demonstrates that the bond character at the interface has a mixed covalent-metallic character that is nonetheless much stronger than the Ag-Ag bond.

In summary, the Ag/Sb-ene interaction exhibits various competing physical and chemical processes, including charge transfer, nontrivial charge redistribution, work function shifts, orbital hybridization, and pushback effects. There are clear indications of changes in the local Sb and Ag chemical environments, and evidence of a moderately strong Sb-Ag interaction. High-resolution XPS measurements on the system may help confirm and clarify these findings.

-
- [1] N. R. Glavin, R. Rao, V. Varshney, E. Bianco, A. Apte, A. Roy, E. Ringe, and P. M. Ajayan, Emerging applications of elemental 2D materials, *Adv. Mater.* **32**, 1904302 (2020).
- [2] S. Zhang, S. Guo, Z. Chen, Y. Wang, H. Gao, J. Gómez-Herrero, P. Ares, F. Zamora, Z. Zhu, and H. Zeng, Recent progress in 2D group-VA semiconductors: From theory to experiment, *Chem. Soc. Rev.* **47**, 982 (2018).
- [3] S. Zhang, M. Xie, F. Li, Z. Yan, Y. Li, E. Kan, W. Liu, Z. Chen, and H. Zeng, Semiconducting group 15 monolayers: A broad range of band gaps and high carrier mobilities, *Angew. Chemie Int. Ed.* **55**, 1666 (2016).
- [4] F. Xia, H. Wang, J. C. M. Hwang, A. H. C. Neto, and L. Yang, Black phosphorus and its isoelectronic materials, *Nat. Rev. Phys.* **1**, 306 (2019).
- [5] M. Pumera and Z. Sofer, 2D monoelemental arsenene, antimonene, and bismuthene: Beyond black phosphorus, *Adv. Mater.* **29**, 1605299 (2017).
- [6] F. Ersan, D. Kecik, V. O. Özçelik, Y. Kadioglu, O. Üzengi Aktürk, E. Durgun, E. Aktürk, and S. Ciraci, Two-dimensional pnictogens: A review of recent progresses and future research directions, *Appl. Phys. Rev.* **6**, 021308 (2019).
- [7] K. S. Novoselov, A. Mishchenko, A. Carvalho, and A. H. Castro Neto, 2D materials and van der Waals heterostructures, *Science* **353**, aac9439 (2016).
- [8] A. K. Geim and I. V. Grigorieva, Van der Waals heterostructures, *Nature (London)* **499**, 419 (2013).
- [9] W. Gao, Z. Zheng, P. Wen, N. Huo, and J. Li, Novel two-dimensional monoelemental and ternary materials: growth, physics and application, *Nanophotonics* **9**, 2147 (2020).
- [10] A. Zhao, H. Li, X. Hu, C. Wang, H. Zhang, J. Lu, S. Ruan, and Y. Zeng, Review of 2D group VA material-based heterostructures, *J. Phys. D: Appl. Phys.* **53**, 293002 (2020).
- [11] C. Grazianetti, C. Martella, and A. Molle, The xenes generations: A taxonomy of epitaxial single-element 2D materials, *Phys. Status Solidi – Rapid Res. Lett.* **14**, 1900439 (2020).
- [12] Z. Wu and J. Hao, Electrical transport properties in group-V elemental ultrathin 2D layers, *npj 2D Mater. Appl.* **4**, 4 (2020).
- [13] W. Zhou, J. Chen, P. Bai, S. Guo, S. Zhang, X. Song, L. Tao, and H. Zeng, Two-dimensional pnictogen for field-effect transistors, *Research* **2019**, 1046329 (2019).
- [14] J. Sturala, Z. Sofer, and M. Pumera, Chemistry of layered pnictogens: phosphorus, arsenic, antimony, and bismuth, *Angew. Chem., Int. Ed.* **58**, 7551 (2019).
- [15] L. Zhang, T. Gong, Z. Yu, H. Dai, Z. Yang, G. Chen, J. Li, R. Pan, H. Wang, Z. Guo, H. Zhang, and X. Fu, Recent advances in hybridization, doping, and functionalization of 2D xenes, *Adv. Funct. Mater.* **31**, 2005471 (2021).
- [16] R. Gusmão, Z. Sofer, D. Bouša, and M. Pumera, Pnictogen (As, Sb, Bi) nanosheets for electrochemical applications are produced by shear exfoliation using kitchen blenders, *Angew. Chem., Int. Ed.* **56**, 14417 (2017).
- [17] D. Zhou, H. Li, N. Si, H. Li, H. Fuchs, and T. Niu, Epitaxial growth of main group monoelemental 2D materials, *Adv. Funct. Mater.* **31**, 2006997 (2021).
- [18] S. Cahangirov, M. Topsakal, E. Aktürk, H. Şahin, and S. Ciraci, Two- and One-Dimensional Honeycomb Structures of Silicon and Germanium, *Phys. Rev. Lett.* **102**, 236804 (2009).
- [19] V. O. Özçelik, E. Durgun, and S. Ciraci, New phases of germanene, *J. Phys. Chem. Lett.* **5**, 2694 (2014).
- [20] Y. Liu, Y. Y. Li, S. Rajput, D. Gilks, L. Lari, P. L. Galindo, M. Weinert, V. K. Lazarov, and L. Li, Tuning Dirac states by strain in the topological insulator Bi_2Se_3 , *Nat. Phys.* **10**, 294 (2014).
- [21] F. Xia, H. Wang, and Y. Jia, Rediscovering black phosphorus as an anisotropic layered material for optoelectronics and electronics, *Nat. Commun.* **5**, 4458 (2014).
- [22] L. Li, Y. Yu, G. J. Ye, Q. Ge, X. Ou, H. Wu, D. Feng, X. H. Chen, and Y. Zhang, Black phosphorus field-effect transistors, *Nat. Nanotechnol.* **9**, 372 (2014).
- [23] J. L. Zhang, S. Zhao, S. Sun, H. Ding, J. Hu, Y. Li, Q. Xu, X. Yu, M. Telychko, J. Su, C. Gu, Y. Zheng, X. Lian, Z. Ma, R. Guo, J. Lu, Z. Sun, J. Zhu, Z. Li, and W. Chen, Synthesis of monolayer blue phosphorus enabled by silicon intercalation, *ACS Nano* **14**, 3687 (2020).
- [24] D. Zhou, Q. Meng, N. Si, X. Zhou, S. Zhai, Q. Tang, Q. Ji, M. Zhou, T. Niu, and H. Fuchs, Epitaxial growth of flat, metallic monolayer phosphorene on metal oxide, *ACS Nano* **14**, 2385 (2020).
- [25] J. Shah, W. Wang, H. M. Sohail, and R. I. G. Uhrberg, Experimental evidence of monolayer arsenene: An exotic 2D semiconducting material, *2D Mater.* **7**, 025013 (2020).
- [26] Z. Zhu and D. Tománek, Semiconducting Layered Blue Phosphorus: A Computational Study, *Phys. Rev. Lett.* **112**, 176802 (2014).
- [27] C. Hogan, K. Holtgrewe, F. Ronci, S. Colonna, S. Sanna, P. Moras, P. M. Sheverdyaeva, S. Mahatha, M. Papagno, Z. S. Aliev, M. Babanly, E. V. Chulkov, C. Carbone, and R. Flammini, Temperature driven phase transition at the

- antimonene/Bi₂Se₃ van der Waals heterostructure, *ACS Nano* **13**, 10481 (2019).
- [28] Zhi-qiang Shi, H. Li, Qian-qian Yuan, Cheng-long Xue, Yongjie Xu, Yang-yang Lv, Zhen-yu Jia, Yanbin Chen, Wenguang Zhu, and Shao-Chun Li, Kinetics-limited two-step growth of van der waals puckered honeycomb Sb monolayer, *ACS Nano* **14**, 16755 (2020).
- [29] D. Zhou, C. Yang, S. Bu, F. Pan, N. Si, P. He, Q. Ji, Y. Lu, and T. Niu, Atomic mechanism of the phase transition in monolayer bismuthene on copper oxide, *Phys. Rev. Mater.* **5**, 064002 (2021).
- [30] D. Zhou, N. Si, B. Jiang, X. Song, H. Huang, Q. Ji, and T. Niu, Interfacial effects on the growth of atomically thin film: Group VA elements on Au(111), *Adv. Mater. Interfaces* **6**, 1901050 (2019).
- [31] M. Gu, C. Li, Y. Ding, K. Zhang, S. Xia, Y. Wang, M.-H. Lu, H. Lu, and Yan-feng Chen, Direct growth of antimonene on C-plane sapphire by molecular beam epitaxy, *Appl. Sci.* **10**, 639 (2020).
- [32] M. Fortin-Deschênes, O. Waller, T. O. Menteş, A. Locatelli, S. Mukherjee, F. Genuzio, P. L. Levesque, A. Hébert, R. Martel, and O. Moutanabbir, Synthesis of antimonene on germanium, *Nano Lett.* **17**, 4970 (2017).
- [33] L. Qiu, J. Dong, and F. Ding, Highly stable phosphorene isomers based on a buckled honeycomb lattice, *Nanoscale* **11**, 7135 (2019).
- [34] J. Zeng, P. Cui, and Z. Zhang, Half Layer By Half Layer Growth of a Blue Phosphorene Monolayer on a GaN(001) Substrate, *Phys. Rev. Lett.* **118**, 046101 (2017).
- [35] N. Han, N. Gao, and J. Zhao, Initial growth mechanism of blue phosphorene on Au(111) surface, *J. Phys. Chem. C* **121**, 17893 (2017).
- [36] P. Giannozzi, S. Baroni, N. Bonini, M. Calandra, R. Car, C. Cavazzoni, D. Ceresoli, G. L. Chiarotti, M. Cococcioni, I. Dabo, A. Dal Corso, S. de Gironcoli, S. Fabris, G. Fratesi, R. Gebauer, U. Gerstmann, C. Gougoussis, A. Kokalj, M. Lazzeri, L. Martin-Samos *et al.*, QUANTUM ESPRESSO: A modular and open-source software project for quantum simulations of materials. *J. Phys.: Condens. Matter* **21**, 395502 (2009).
- [37] M. J. van Setten, M. Giantomassi, E. Bousquet, M. J. Verstraete, D. R. Hamann, X. Gonze, and G.-M. Rignanese, The PseudoDojo : Training and grading a 85 element optimized norm-conserving pseudopotential table, *Comput. Phys. Commun.* **226**, 39 (2018).
- [38] D. R. Hamann, Optimized norm-conserving Vanderbilt pseudopotentials, *Phys. Rev. B* **88**, 085117 (2013).
- [39] S. Haastrup, M. Strange, M. Pandey, T. Deilmann, P. S. Schmidt, N. F. Hinsche, M. N. Gjerding, D. Torelli, P. M. Larsen, A. C. Riis-Jensen, J. Gath, K. W. Jacobsen, J. Jørgen Mortensen, T. Olsen, and K. S. Thygesen, The computational 2D materials database: High-throughput modeling and discovery of atomically thin crystals, *2D Mater.* **5**, 042002 (2018).
- [40] J. Zhou, L. Shen, M. D. Costa, K. A. Persson, S. P. Ong, P. Huck, Y. Lu, X. Ma, Y. Chen, H. Tang, and Y. P. Feng, 2DMatPedia, an open computational database of two-dimensional materials from top-down and bottom-up approaches, *Sci. data* **6**, 86 (2019).
- [41] P. J. Kowalczyk, O. Mahapatra, M. Le Ster, S. A. Brown, G. Bian, X. Wang, and T.-C. Chiang, Single atomic layer allotrope of bismuth with rectangular symmetry, *Phys. Rev. B* **96**, 205434 (2017).
- [42] F. Ersan, E. Aktürk, and S. Ciraci, Stable single-layer structure of group-V elements, *Phys. Rev. B* **94**, 245417 (2016).
- [43] S. Singh, Z. Zanolli, M. Amsler, B. Belhadji, J. O. Sofo, M. J. Verstraete, and A. H. Romero, Low-energy phases of Bi monolayer predicted by structure search in two dimensions, *J. Phys. Chem. Lett.* **10**, 7324 (2019).
- [44] W. H. Han, Sunghyun Kim, I. H. Lee, and K. J. Chang, Prediction of green phosphorus with tunable direct band gap and high mobility, *J. Phys. Chem. Lett.* **8**, 4627 (2017).
- [45] T. Kaewmaraya, L. Ngamwongwan, P. Moontragoon, W. Jareenboon, D. Singh, R. Ahuja, A. Karton, and T. Hussain, Novel green phosphorene as a superior chemical gas sensing material, *J. Hazard. Mater.* **401**, 123340 (2021).
- [46] J. P. Perdew, K. Burke, and M. Ernzerhof, Generalized Gradient Approximation Made Simple, *Phys. Rev. Lett.* **77**, 3865 (1996).
- [47] D. Tristant, A. Cupo, and V. Meunier, Finite temperature stability of single-layer black and blue phosphorus adsorbed on Au(1 1 1): a first-principles study, *2D Mater.* **5**, 035044 (2018).
- [48] S. Grimme, Semiempirical GGA-type density functional constructed with a long-range dispersion correction, *J. Comput. Chem.* **27**, 1787 (2006).
- [49] T. Thonhauser, S. Zuluaga, C. A. Arter, K. Berland, E. Schröder, and P. Hyldgaard, Spin Signature of Nonlocal Correlation Binding in Metal-Organic Frameworks, *Phys. Rev. Lett.* **115**, 136402 (2015).
- [50] T. Thonhauser, V. R. Cooper, S. Li, A. Puzder, P. Hyldgaard, and D. C. Langreth, Van der Waals density functional: Self-consistent potential and the nature of the van der Waals bond, *Phys. Rev. B* **76**, 125112 (2007).
- [51] M. Dion, H. Rydberg, E. Schröder, D. C. Langreth, and B. I. Lundqvist, Van der Waals Density Functional for General Geometries, *Phys. Rev. Lett.* **92**, 246401 (2004).
- [52] K. Lee, É. D. Murray, L. Kong, B. I. Lundqvist, and D. C. Langreth, Higher-accuracy van der Waals density functional, *Phys. Rev. B* **82**, 081101(R) (2010).
- [53] R. Sabatini, E. Küçükbenli, B. Kolb, T. Thonhauser, and S. de Gironcoli, Structural evolution of amino acid crystals under stress from a non-empirical density functional, *J. Phys.: Condens. Matter* **24**, 424209 (2012).
- [54] J. Klimeš, D. R. Bowler, and A. Michaelides, Van der Waals density functionals applied to solids, *Phys. Rev. B* **83**, 195131 (2011).
- [55] I. Hamada, van der Waals density functional made accurate, *Phys. Rev. B* **89**, 121103(R) (2014).
- [56] F. Tran, L. Kalantari, B. Traoré, X. Rocquefelte, and P. Blaha, Nonlocal van der Waals functionals for solids: Choosing an appropriate one, *Phys. Rev. Mater.* **3**, 063602 (2019).
- [57] Y. Kadioglu, J. A. Santana, H. Duygu Özyaydin, F. Ersan, O. İzengi Aktürk, E. Aktürk, and F. A. Reboredo, Diffusion quantum Monte Carlo and density functional calculations of the structural stability of bilayer arsenene, *J. Chem. Phys.* **148**, 214706 (2018).
- [58] G. R. Qian, X. Dong, X. F. Zhou, Y. Tian, A. R. Oganov, and H. T. Wang, Variable cell nudged elastic band method for studying solid-solid structural phase transitions, *Comput. Phys. Commun.* **184**, 2111 (2013).
- [59] G. Henkelman, B. P. Uberuaga, and H. Jónsson, Climbing image nudged elastic band method for finding saddle

- points and minimum energy paths, *J. Chem. Phys.* **113**, 9901 (2000).
- [60] C. W. Glass, A. R. Oganov, and N. Hansen, USPEX-Evolutionary crystal structure prediction, *Comput. Phys. Commun.* **175**, 713 (2006).
- [61] S.-Y. Zhu, Y. Shao, E. Wang, L. Cao, X.-Y. Li, Z.-L. Liu, C. Liu, L.-W. Liu, J.-O. Wang, K. Ibrahim, J.-T. Sun, Y.-L. Wang, S. Du, and H.-J. Gao, Evidence of topological edge states in buckled antimonene monolayers, *Nano Lett.* **19**, 6323 (2019).
- [62] F. Therrien, P. Graf, and V. Stevanović, Matching crystal structures atom-to-atom, *J. Chem. Phys.* **152**, 074106 (2020).
- [63] J. Carrete, L. J. Gallego, and N. Mingo, Structural complexity and phonon physics in 2D arsenenes, *J. Phys. Chem. Lett.* **8**, 1375 (2017).
- [64] R. Flammini, S. Colonna, C. Hogan, S. K. Mahatha, M. Papagno, A. Barla, P. M. Sheverdyayeva, P. Moras, Z. S. Aliev, M. B. Babanly, E. V. Chulkov, C. Carbone, and F. Ronci, Evidence of β -antimonene at the Sb/Bi₂Se₃ interface, *Nanotechnology* **29**, 065704 (2018).
- [65] J. Gao, G. Zhang, and Y.-W. Zhang, The critical role of substrate in stabilizing phosphorene nanoflake: A theoretical exploration, *J. Am. Chem. Soc.* **138**, 4763 (2016).
- [66] Y. Shao, Z.-L. L. Liu, C. Cheng, X. Wu, H. Liu, C. Liu, J.-O. O. Wang, Shi-yu Yu Zhu, Yu-Qi Qi Ye-liang Liang Wang, Dong-xia Xia Shi, K. Ibrahim, Jia-tao Tao Sun, Yu-Qi Qi Ye-liang Liang Wang, and Hong-jun Jun Gao, Epitaxial growth of flat antimonene monolayer: A new honeycomb analogue of graphene, *Nano Lett.* **18**, 2133 (2018).
- [67] J. Mao and Y. Chen, Band engineering and hybridization of competing arsenene allotropes: a computational study, *Phys. Chem. Chem. Phys.* **21**, 24499 (2019).
- [68] J. Wang, T. Yang, Z. Zhang, and L. Yang, Enhanced doping effect on tuning structural phases of monolayer antimony, *Appl. Phys. Lett.* **112**, 213104 (2018).
- [69] D. Zhou, H. Li, S. Bu, B. Xin, Y. Jiang, N. Si, J. Sun, Q. Ji, H. Huang, H. Li, and T. Niu, Phase engineering of epitaxial stanene on a surface alloy, *J. Phys. Chem. Lett.* **12**, 211 (2021).
- [70] T. Nagao, J. T. Sadowski, M. Saito, S. Yaginuma, Y. Fujikawa, T. Kogure, T. Ohno, Y. Hasegawa, S. Hasegawa, and T. Sakurai, Nanofilm Allotrope and Phase Transformation of Ultrathin Bi Film on Si(111)-7 \times 7, *Phys. Rev. Lett.* **93**, 105501 (2004).
- [71] F. He, E. S. Walker, Y. Zhou, R. D. Montano, S. R. Bank, and Y. Wang, Phase transition in epitaxial bismuth nanofilms, *Appl. Phys. Lett.* **117**, 073103 (2020).
- [72] M. Fortin-Deschênes, H. Zschiesche, T. O. Menteş, A. Locatelli, R. M. Jacobberger, F. Genuzio, M. J. Lagos, D. Biswas, C. Jozwiak, J. A. Miwa, S. Ulstrup, A. Bostwick, E. Rotenberg, M. S. Arnold, G. A. Botton, and O. Moutanabbir, Pnictogens allotropy and phase transformation during van der Waals growth, *Nano Lett.* **20**, 8258 (2020).
- [73] See <http://www.2dmatpedia.org/2dmaterials/doc/2dm-4275>.
- [74] See <https://www.materialsproject.org/materials/mp-567409/>.
- [75] S. Yaginuma, K. Nagaoka, T. Nagao, G. Bihlmayer, Y. M. Koroteev, E. V. Chulkov, and T. Nakayama, Electronic structure of ultrathin bismuth films with A7 and black-phosphorus-like structures, *J. Phys. Soc. Jpn.* **77**, 014701 (2008).
- [76] A. Lopez-Bezanilla, Effect of atomic-scale defects and dopants on phosphorene electronic structure and quantum transport properties, *Phys. Rev. B* **93**, 035433 (2016).
- [77] Wei Zhang, Hanna Enriquez, Yongfeng Tong, Azzedine Bendounan, Abdelkader Kara, Ari P. Seitsonen, Andrew J. Mayne, Gérald Dujardin, and Hamid Oughaddou, Epitaxial synthesis of blue phosphorene, *Small* **14**, 1804066 (2018).
- [78] J.-P. Xu, J.-Q. Zhang, H. Tian, H. Xu, W. Ho, and M. Xie, One-dimensional phosphorus chain and two-dimensional blue phosphorene grown on Au(111) by molecular-beam epitaxy, *Phys. Rev. Mater.* **1**, 061002(R) (2017).
- [79] K. Holtgrewe, C. Hogan, and S. Sanna, Evolution of topological surface states following Sb layer adsorption on Bi₂Se₃, *Materials* **14**, 1763 (2021).
- [80] K. Holtgrewe, S. K. Mahatha, P. M. Sheverdyayeva, P. Moras, R. Flammini, S. Colonna, F. Ronci, M. Papagno, A. Barla, L. Petaccia, Z. S. Aliev, M. B. Babanly, E. V. Chulkov, S. Sanna, C. Hogan, and C. Carbone, Topologization of β -antimonene on Bi₂Se₃ via proximity effects, *Sci. Rep.* **10**, 14619 (2020).
- [81] M. Jałochowski and M. Krawiec, Antimonene on Pb quantum wells, *2D Mater.* **6**, 045028 (2019).
- [82] Z.-Q. Shi, H. Li, Q.-Q. Yuan, Y.-H. Song, Y.-Y. Lv, W. Shi, Z.-Y. Jia, L. Gao, Y.-B. Chen, W. Zhu, and S.-C. Li, Van der Waals heteroepitaxial growth of monolayer Sb in a puckered honeycomb structure, *Adv. Mater.* **31**, 1806130 (2019).
- [83] Z.-Q. Shi, H. Li, C.-L. Xue, Q.-Q. Yuan, Y.-Y. Lv, Y.-J. Xu, Z.-Y. Jia, L. Gao, Y. Chen, W. Zhu, and S.-C. Li, Tuning the electronic structure of an α -antimonene monolayer through interface engineering, *Nano Lett.* **20**, 8408 (2020).
- [84] T. Märkl, P. J. Kowalczyk, M. Le Ster, I. V. Mahajan, H. Pirie, Z. Ahmed, G. Bian, X. Wang, T.-C. Chiang, and S. A. Brown, Engineering multiple topological phases in nanoscale Van der Waals heterostructures: Realisation of α -antimonene, *2D Mater.* **5**, 011002 (2017).
- [85] T. Niu, W. Zhou, D. Zhou, X. Hu, S. Zhang, K. Zhang, M. Zhou, H. Fuchs, and H. Zeng, Modulating epitaxial atomic structure of antimonene through interface design, *Adv. Mater.* **31**, 1902606 (2019).
- [86] T. Niu, Q. Meng, D. Zhou, N. Si, S. Zhai, X. Hao, M. Zhou, and H. Fuchs, Large-scale synthesis of strain-tunable semiconducting antimonene on copper oxide, *Adv. Mater.* **32**, 1906873 (2020).
- [87] F. Ersan and E. Aktürk and S. Ciraci, Stable, one-dimensional suspended and supported monatomic chains of pnictogens: A metal-insulator framework, *Phys. Chem. Chem. Phys.* **21**, 14832 (2019).
- [88] K. Momeni, Y. Ji, Y. Wang, S. Paul, S. Neshani, D. E. Yilmaz, Y. K. Shin, D. Zhang, J.-W. Jiang, H. S. Park, S. Sinnott, A. Duin, V. Crespi, L.-Q. Chen, Multiscale computational understanding and growth of 2D materials: a review, *npj Comput. Mater.* **6**, 22 (2020).
- [89] M. Le Ster, T. Maerkl, P. J. Kowalczyk, and S. A. Brown, Moiré patterns in van der Waals heterostructures, *Phys. Rev. B* **99**, 075422 (2019).
- [90] X. Wu, Y. Shao, H. Liu, Z. Feng, Y.-L. Wang, J.-T. Sun, C. Liu, J.-O. Wang, Z.-L. Liu, S.-Y. Zhu, Y.-Q. Wang, S.-X. Du, Y.-G. Shi, K. Ibrahim, and H.-J. Gao, Epitaxial growth and air-stability of monolayer antimonene on PdTe₂, *Adv. Mater.* **29**, 1605407 (2017).
- [91] T. Lei, C. Liu, J.-L. Zhao, J.-M. Li, Y.-P. Li, J.-O. Wang, R. Wu, H.-J. Qian, H.-Q. Wang, and K. Ibrahim, Electronic structure of antimonene grown on Sb₂Te₃ (111) and Bi₂Te₃ substrates, *J. Appl. Phys.* **119**, 015302 (2016).

- [92] S. Sun, T. Yang, Y. Z. Luo, J. Gou, Y. Huang, C. Gu, Z. Ma, X. Lian, S. Duan, A. T. S. Wee, M. Lai, J. L. Zhang, Y. P. Feng, and W. Chen, Realization of a buckled antimonene monolayer on Ag(111) via surface engineering, *J. Phys. Chem. Lett.* **11**, 8976 (2020).
- [93] Y. Lu, W. Xu, M. Zeng, G. Yao, L. Shen, M. Yang, Z. Luo, F. Pan, K. Wu, T. Das, P. He, J. Jiang, J. Martin, Y. P. Feng, H. Lin, and X. S. Wang, Topological properties determined by atomic buckling in self-assembled ultrathin Bi(110), *Nano Lett.* **15**, 80 (2015).
- [94] P. J. Kowalczyk, S. A. Brown, T. Maerkl, Q. Lu, C.-K. Chiu, Y. Liu, S. A. Yang, X. Wang, I. Zasada, F. Genuzio, T. O. Menteş, A. Locatelli, T.-C. Chiang, and G. Bian, Realization of symmetry-enforced two-dimensional dirac fermions in non-symmorphic α -bismuthene, *ACS Nano* **14**, 1888 (2020).
- [95] F. Yang, L. Miao, Z. F. Wang, M.-Y. Yao, F. Zhu, Y. R. Song, M.-X. Wang, J.-P. Xu, A. V. Fedorov, Z. Sun, G. B. Zhang, C. Liu, F. Liu, D. Qian, C. L. Gao, and J.-F. Jia, Spatial and Energy Distribution of Topological Edge States in Single Bi(111) Bilayer, *Phys. Rev. Lett.* **109**, 016801 (2012).
- [96] S. H. Kim, K.-H. Jin, J. Park, J. S. Kim, S.-H. Jhi, T.-H. Kim, and H. W. Yeom, Edge and interfacial states in a two-dimensional topological insulator: Bi(111) bilayer on Bi₂Te₂Se₃, *Phys. Rev. B* **89**, 155436 (2014).
- [97] F. Reis, G. Li, L. Dudy, M. Bauernfeind, S. Glass, W. Hanke, R. Thomale, J. Schäfer, and R. Claessen, Bismuthene on a SiC substrate: A candidate for a high-temperature quantum spin Hall material, *Science* **357**, 287 (2017).